Direct Numerical Simulation of Starting-Plume Cloud-Flows

A Thesis

Submitted for the Degree of

MASTER OF SCIENCE (ENGINEERING)

in the Faculty of Engineering

by

KONDURI ADITYA

ENGINEERING MECHANICS UNIT
JAWAHARLAL NEHRU CENTRE FOR ADVANCED SCIENTIFIC RESEARCH
(A Deemed University)
Bangalore – 560 064

AUGUST 2009

To my parents and Prof. R. Narasimha

DECLARATION

I hereby declare that the matter embodied in the thesis entitled "**Direct Numercial Simulation of Starting-Plume Cloud-Flows**" is the result of investigations carried out by me at the Engineering Mechanics Unit, Jawaharlal Nehru Centre for Advanced Scientific Research, Bangalore, India under the supervision of Prof. Roddam Narasimha and Prof. K. R. Sreenivas and that it has not been submitted elsewhere for the award of any degree or diploma.

In keeping with the general practice in reporting scientific observations, due acknowledgment has been made whenever the work described is based on the findings of other investigators.

Konduri Aditya

CERTIFICATE

I hereby certify that the matter embodied in this thesis entitled "**Direct Numercial Simulation of Starting-Plume Cloud-Flows**" has been carried out by Mr. Konduri Aditya at the Engineering Mechanics Unit, Jawaharlal Nehru Centre for Advanced Scientific Research, Bangalore, India under my supervision and that it has not been submitted elsewhere for the award of any degree or diploma.

Prof. Roddam Narasimha	Prof. K. R. Sreenivas
(Research Supervisor)	(Research Supervisor)

Acknowledgements

Firstly, I thank my advisors Prof. R. Narasimha, Prof. K. R. Sreenivas and Prof. S. M. Deshpande for giving me an opportunity to work with them.

It has been a great pleasure to be a student of Prof. Narasimha, who has not only been my advisor but also a mentor and a fatherly figure to me. This thesis would not have taken the present form without his constant encouragement and support. He was always ready to answer my queries, and I remember calling him late in the night many times to get my doubts cleared which he did not mind and in fact responded to cheerfully. He was a patient listener and would give me his best possible advice. His approach towards tackling scientific problems has left a deep impression on my mind. I have thoroughly enjoyed all the time spend with him, and I cherish the lunch table discussions with him which many a times went beyond fluid dynamics into as diverse topics as politics, history and philosophy. I feel myself fortunate to have been associated with him.

My first entry into JNC was made possible by Prof. Sreenivas when I worked with him during my undergraduate days. This period was crucial as it got me interested in studying fluid mechanics further which eventually led me to come to JNC for my Master's degree. He gave me the freedom to work on the topic of my interest. His constructive criticism and suggestions in our discussions have proved valuable to me. I am grateful to him for all his kind help.

I owe thanks to Prof. Deshpande who accepted my request to offer a course in CFD which introduced me to the computational techniques and later on guided me in development of the DNS code. He also gave me access to the Dell workstation, which enabled me to carry out the initial simulations.

I acknowledge Tata CRL, Pune for providing me the supercomputing facility (Eka) to carry out the simulations, and I thank the CFD group at CRL for helping me to use the facility.

My parents have been very supportive in my pursuit of higher studies and encouraged me to take up a career in research. I thank my parents and sister for their unlimited patience and support.

The courses taught by Prof. Rama Govindarajan, Prof. G. S. Bhat and Prof. J. Srinivasan have greatly helped me in preparing the necessary technical background to carry out my work.

Thanks are due to Ms. Nagarathna for extending a hand of support, especially in writing up of my thesis. She also helped me to appreciate the nuances of carnatic music, and the concerts which I attended with her are some of the memorable experiences during my stay at Bangalore.

I relish the delightful discussions with Prof. Garry Brown during his visit to EMU.

I thank my labmates Anubhab, Ashish, Devaranjan, Dhiraj, Dinesh, Harish, Gayathri, Ponnu, Rahul, Rajapandiyan, Rakshith, Ratul, Subrahmanyam, Sujan, Sumesh, Vivekanand and others for extending necessary help whenever needed.

I thank Rajaram for spending valuable time in making me understand different aspects of my work and giving necessary directions. I thank my friends Bharath, Gopikrishna, Nikhil, Shyam Prasad and Sushmita for constantly keeping in touch with me during my stay at JNC.

I owe a ton to Sourabh Diwan, who helped me with the data analysis and writing up of my thesis. It would have been impossible for me to finish the thesis in time without his support.

The acknowledgment will be incomplete if I don't thank Vivek Prakash, who is my roommate, labmate and a great friend. Life at JNC would have been colourless without his company. His constant support and advice on several issues have helped me in carrying on with life at JNC smoothly and I am grateful to him.

Contents

Abstract

In the present work, we study the effect of off-source volumetric heating on a starting plume in an attempt to understand the fluid dynamics of clouds. Clouds play a major role in weather and climate. In the tropics cumulus clouds are particularly prominent. They generally form due to condensation of water vapor in the moist air that rises from heat sources or hot spots on the ground. Previous work (as reviewed by Narasimha & Bhat (2008))has shown that off-source volumetric heating of a self-similar jet or a plume results in cloud like flow characteristics. A starting plume is particularly relevant to clouds as the life cycle time of a single cloud is of the order of a few hours and is usually not long enough to generate completely self-similar flows. We carry out Direct Numerical Simulation (DNS) of the Navier-Stokes equations under the Boussinesq approximation to study such flows.

We start with two-dimensional (2D) simulations to explore suitable algorithms and boundary conditions. A clustered Cartesian grid is used for the computation. The equations are solved using the projection method and finite difference schemes. For integration in time, second order Adams-Bashforth and Crank-Nicolson methods are used for advection and viscous diffusion respectively. The code is verified by demonstrating conservation of buoyancy flux and satisfaction of the divergence-free condition. The 2D simulation of the starting-plume model gives results broadly similar to those seen in the experiments on round jets and plumes. In the heat-injection zone the spread rate of the plume decreases. Immediately above the heat-injection zone instabilities begin to reappear and the spread rate tends to recover.

As the simulations in 2D showed promise, we started developing a three dimensional (3D) DNS code. A cylindrical domain is chosen for the computation, as the flow is axisymmetric in the mean. The governing equations in cylindrical coordinates possess a geometric singularity at the axis, $r = 0$. A method proposed

by Verzicco & Orlandi (1996) is used to overcome this problem. The algorithm and numerical schemes used for 3D simulations are basically same as in 2D. In this type of flow, where the entrainment at the flow boundaries is of interest, the issue of boundary conditions assumes utmost importance. We have experimented with different boundary conditions and found zero vorticity at the lateral boundary and zero normal derivatives at the outflow to be most appropriate. As the calculations are computationally intensive, we have parallelized the code using the domain decomposition technique and run it on the Tata's super-computer Eka at CRL, Pune. To the best of our knowledge no results on starting plumes with or without off-source heating have been reported, and hence the validation of the code is not possible; therefore we have verified it according to the appropriate conservation principles (as done in 2D simulations). Results are reported here for a grid resolution of $100 \times 100 \times 100$ and it has been observed that heat addition leads to dramatic changes in the structure of the plume. In the Heat-Injection Zone (HIZ), there is a drastic decrease in the stream-wise vorticity component as the amount of heat added increases. The values of azimuthal velocity, whose mean is zero, are an indication of turbulent fluctuations. It is found that heating leads to decay of azimuthal fluctuating velocities suggesting relaminarization-like behaviour of the flow in HIZ.

Nomenclature

d_0	:	Heat source diameter
T_0	:	Heat source temperature over ambient
z	:	Vertical direction
t	:	Time
z_b	:	Beginning of the heat injection zone
z_t	:	End of the heat injection zone
$\boldsymbol{u}$	:	Velocity vector
T	:	Change in temperature over ambient
p	:	Pressure
ρ	:	Density
J	:	Heat added per unit volume per unit time
C_p	:	Specific heat at constant pressure
ν	:	Kinematic viscosity
α	:	Coefficient of thermal expansion
κ	:	Thermal diffusivity
g	:	Acceleration due to gravity
$\hat{z}$	:	Unit vector in vertically upward direction
H	:	Off-source heat addition function
T_{limit}	:	Threshold temperature to identify heating area
U_o	:	The velocity scale used for non-dimensionalisation
Re	:	Reynolds number
Pr	:	Prandtl number
G	:	Heat Release Number
Ri	:	Richardson number
n	:	Time step index

Δt	:	Time increment
$\tilde{u}^{n+1}$	:	Intermediate velocity in the projection method
ϕ^{n+1}	:	$p^{n+1} - p^n$
x	:	Cross-stream direction (2D)
y	:	Streamwise direction (2D)
x_{max}	:	Maximum length in x direction (2D)
ξ, η	:	Transformed co-ordinates corresponding to x and y respectively (2D)
r	:	Radial direction (3D)
θ	:	Azimuthal direction (3D)
i	:	Index for x direction (2D) and θ direction (3D)
j	:	Index for y direction (2D) and r direction (3D)
k	:	Index for z direction (3D)
q	:	Dependent variable used in 3D simulations related to the velocity field
t^*	:	Non-dimensional time
jp, kp	:	Number of sub-domains along r and z directions respectively in the parallel architecture
np	:	Total number of processors

List of Figures

List of Tables

CHAPTER 1

INTRODUCTION

Cumulus clouds are fluffy clouds which sometimes look like pieces of floating cotton in the sky. These are prominently seen especially in the tropics, with flat bases and tops sometimes reaching high up into the atmosphere like towers, all the way to the tropopause or even beyond (nearly 15km). Figure 1.1(a) is a picture of natural clouds and figure 1.1(b) is an image from a dye flow visualization of a jet subjected to off-source volumetric heating evolving in an ambient fluid whose density is discontinuous at the level where the jet spreads out horizontally (Narasimha & Bhat (2008)). The remarkable resemblance between real clouds in the sky and the laboratory jet with off-source heating indicates that one of the major dynamical influence on a cumulus cloud is heat released during condensation of the water vapor. With this motivation we study the fluid dynamics of clouds further.

Figure 1.1: (a) Natural clouds. (b) Laboratory flow visualization of a jet subjected to off-source volumetric heating in a discontinuously stratified environment. (Narasimha & Bhat (2008))

Cloud formation begins typically with moist air near some hot spot on the surface rising up into the atmosphere by convection. During the ascent, the moist air parcel undergoes an adiabatic expansion with a drop in its temperature. When this parcel is sufficiently saturated with water vapour, its further ascent leads to the condensation of excess water vapour into liquid drops or ice particles forming a cloud. The shape of a cloud is mainly influenced by the amount of latent heat released, stratification due to density variation of air in the atmosphere and cross winds.

In a fluid dynamical perspective, the flow involved in a cloud formation and growth can be seen as a natural turbulent shear flow, and can be more specifically put into the class of thermals and plumes (Turner (1973)). The evolution of a cloud flow is different from a classical plume as it is imparted with additional buoyancy force away from the surface due to the latent heat released during condensation of water vapour. The behaviour of an ordinary plume has been studied extensively and reviewed in Turner (1969) and List (1982). One major feature in this type of a shear flow is the entrainment of ambient fluid through lateral edges. In case of a turbulent plume, the ambient fluid is continuously engulfed into the core fluid by the large eddies followed by rapid small scale mixing across the core with constant entrainment coefficient (Turner (1986)).

The plume models based on the entrainment hypothesis of Taylor (Morton *et al.* (1956)), which have been successful in predicting flow development in a variety of geophysical situations (Turner (1986)), fail to make realistic estimates of either liquid-water concentrations or height of penetration in clouds (Squires & Turner (1962) and Warner (1970)). From measurements of the temperature and liquid-water concentration in tall Colorado cumuli using an aircraft, Paluch (1979) inferred that the entrainment of ambient air from the sides may be very small in

tall cumulus clouds. This study showed that the observed cloud thermodynamic properties can be accounted for only if air from the cloud base ascends to the top without laterally mixing with the surrounding air. Similar observations on cumulonimbus clouds in the tropics have been reported by Riehl (1972). A summary of the earlier ideas on entrainment and mixing processes in clouds has been given in Simpson (1983). Emanuel (1994) pointed out that early cloud parameterization schemes based on plume entrainment model are not in agreement with observations.

A new approach to study the fluid dynamics of clouds started with the experiments carried out at the Centre for Atmospheric Sciences, Indian Institute of Science in Bangalore. A novel technique has been developed to study the effect of locally enhanced buoyancy by volumetric heating of a shear flow (jet/plume) (Bhat *et al.* (1989)). The volumetric heat has been achieved by ohmic heating of water which is made electrically conducting by adding small quantities of acid and using non-conducting deionized water as the ambient fluid. Elavarasan *et al.* (1995) reported an exploratory study of the flow using this setup and a detailed analysis is given in Bhat & Narasimha (1996). Flow visualization using Laser-Induced-Fluorescence (LIF) has revealed a drastic reduction in the jet spread rate due to heating. It has been observed that the coherent eddy structures get disrupted in the heat-injection zone leading to a relative reduction in entrainment. Based on such observations an entrainment model for clouds has been proposed. Similar investigations have been reported by Agrawal & Prasad (2004) and Venkatakrishnan *et al.* (2003). In their Particle-Image-Velocimetry (PIV) measurements, Agrawal & Prasad (2004) have found similar observations due to heating as in Bhat & Narasimha (1996) except for the normalized turbulent intensity. Narasimha & Bhat (2008) reanalyzed the data from all the three groups and summarized the current status of the problem. They attributed the disagreement in normalized

turbulent intensity to higher electrical conductivity of jet fluid in Agrawal's experiments.

A plume is a buoyancy driven flow and is a better analogy for cloud flow than a jet, which is momentum driven. Experiments on a self-similar plume subjected to off-source heating have shown characteristics similar to discussed above (Venkatakrishnan *et al.* (1999)).

A two-dimensional theoretical model for entrainment in jet and plumes (with and with out off-source heating) is given in Sreenivas & Prasad (2000). They explain the entrainment process based on vortex-dynamics principles and the effect of the baroclinic torque (due to stratification in the flow) on large scale structures. In a plume, the density stratification in the core flow is unstable and results in a baroclinic torque enhancing the formation of eddy structure. As a result, the entrainment in a plume is greater than in a jet. Off-source heating creates a stable stratification in the core flow of a plume which decreases the eddy formation, thereby reducing the entrainment when compared to an unheated plume. Based on this model Sreenivas (2004) studied the effect of acceleration on the entrainment process in a planar jet, by carrying out simulations using diffusion-vortex method. The result indicates reduction in entrainment with axial acceleration.

In addition to the experiments, attempts have also been made to simulate the flow by solving the Navier-Stokes equations using Direct Numerical Simulation (DNS) in which all the characteristics are computed in detail. The simulation of free shear flows like jets and plumes is found to be difficult as they evolve in a space with no clear boundaries. A major challenge lies in accurate computation of the entrainment flow field. DNS of incompressible round jets have been extensively studied (Boersma *et al.* (1998) and Babu & Mahesh (2004)). A recent simulation of a turbulent plume solved under the low mach number approximation is due to

Plourde *et al.* (2008). In their solutions they observe periodic generation of vortex rings near the heat source. The rings then travel downstream, interact with the core flow and destabilize it leading to a turbulent flow field. They have also looked at the instantaneous entrainment process in the plume in great detail. According to them, the entrainment process consists of local contraction and expulsion phases, which result in large fluctuations of instantaneous entrainment coefficient both in space and time. Basu & Narasimha (1999) carried out a temporal simulation using spectral methods in a periodic domain. The results obtained from their computation are qualitatively in agreement with the experiments and have further shown that heating leads to dramatic increase in the vorticity and its gradients in the flow. A spatially evolving jet with enhanced buoyancy has been simulated by Agrawal *et al.* (2004). In this simulation, the governing equations are solved in a spherical coordinate system with a traction-free condition for lateral boundary and convective boundary condition at the outflow. The amount of off-source heat introduced in the flow is proportional to a scalar concentration obtained by solving an advection-diffusion equation. The value of their Richardson number is nearly 40 times higher than in experiments and real clouds.

Turner (1973) has pointed out that a starting plume may be more relevant to modelling clouds as the life cycle time of a single cloud is of the order of a few hours, usually not long enough to generate completely self-similar flows. To the best of our knowledge no results on starting plumes with or without off-source heating have been reported. In the present work we investigate a starting-plume flow subjected to off-source volumetric heating as a model for cloud flow using Direct Numerical Simulation (DNS) technique.

This thesis is structured as follows: In chapter 2 the governing equations, computational details, and parallelization details are outlined. The results obtained

from 2D simulations have been presented in Chapter 3. Chapter 4 deals with the 3D simulations of axisymmetric plumes. The conclusions from the present work and future work are outlined in Chapter 5.

CHAPTER 2

COMPUTATIONAL METHOD

2.1 Flow Configuration

As discussed in chapter 1, we investigate in this thesis whether a cumulus cloud flow can be simulated using a starting plume with off-source volumetric heating. A schematic of the flow under consideration is shown in figure 2.1. The configuration consists of a starting plume rising from a heat source (e.g. hot spot on the ground) of diameter d_0, whose temperature is T_0 over the ambient temperature. As the plume reaches the Heat-Injection Zone (HIZ) which begins at a height z_b and ends at z_t, it is subjected to off-source volumetric heating. The amount of heat injected in HIZ is to be made dynamically similar to the latent heat released during condensation of water vapour in the cloud.

2.2 Governing Equations

It is assumed that the density changes in the flow due to heating are very small and the effect of change in density appears only as a buoyancy term in the momentum equation. Thus the flow is governed by the incompressible Navier-Stokes equations under the Boussinesq approximation and with off-source heat addition as proposed in Basu & Narasimha (1999).

Continuity:

$$\bigtriangledown . \boldsymbol{u} = 0 \tag{2.1}$$

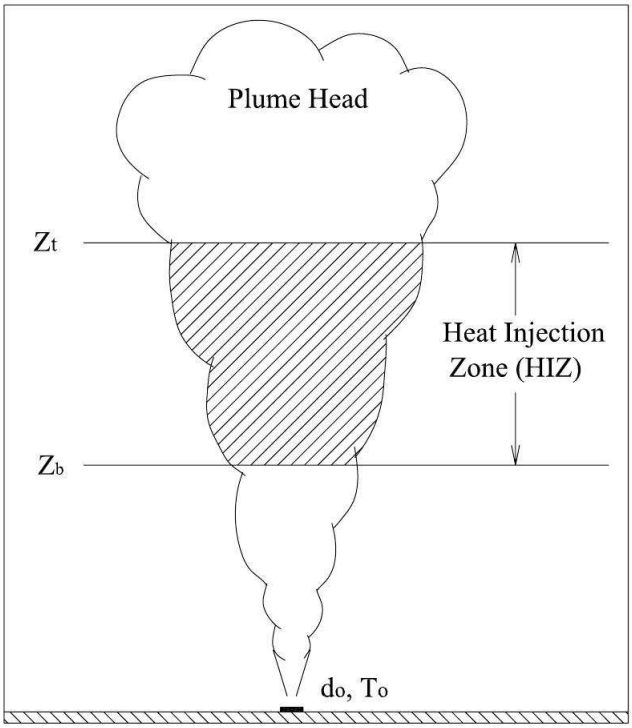

Figure 2.1: A schematic of a starting plume with off-source volumetric heating.

Momentum:

$$\frac{\partial \boldsymbol{u}}{\partial t} + \boldsymbol{u}.\nabla \boldsymbol{u} = -\frac{1}{\rho}\nabla p + \nu.\nabla^2 \boldsymbol{u} - \boldsymbol{g}\alpha T \tag{2.2}$$

Energy:

$$\frac{\partial T}{\partial t} + \boldsymbol{u}.\nabla T = \kappa \nabla^2 T + \frac{J}{\rho C_p} H(z, r, t) \tag{2.3}$$

Here $\boldsymbol{u}$ is the velocity vector, T the change in temperature above ambient, p the pressure, ρ the density, J the heat added per unit volume per unit time, C_p the specific heat at constant pressure, ν the kinematic viscosity, α the coefficient of thermal expansion and κ the thermal diffusivity. The acceleration due to gravity $\boldsymbol{g}$ acts vertically downwards and is given by $\boldsymbol{g} = -g\widehat{z}$, where $\widehat{z}$ is the unit vector in the vertically upward direction. The off-source heat is added according to the function $H(z, r, t)$ defined as follows.

$$H(z,r,t) = 1 \text{ for } z_b \leq z \leq z_t,\ T(z,r,t) \geq T_{limit}$$
$$= 0 \text{ else where}$$

Here, T_{limit} is a threshold used to identify the off-source heating area at a particular height in the HIZ.

2.3 Non-dimensional Equations and Numbers

The governing equations are non-dimensionalized using the heat source diameter d_0 as the length scale and heat source temperature T_0 as the temperature scale. The velocity scale is obtained as $U_0 = \sqrt{g\alpha T_0 d_0}$. The equations in the non-dimensional variables (indicated with asterisk) are as follows:

$$\nabla^* . \boldsymbol{u}^* = 0 \tag{2.4}$$

$$\frac{\partial \boldsymbol{u}^*}{\partial t^*} + \boldsymbol{u}^* . \nabla^* \boldsymbol{u}^* = -\nabla^* p^* + \frac{1}{Re} \nabla^{*2} \boldsymbol{u}^* - T^* \hat{z} \tag{2.5}$$

$$\frac{\partial T^*}{\partial t^*} + \boldsymbol{u}^* . \nabla^* T^* = \frac{1}{RePr} \nabla^{*2} T^* + GH(z,r,t) \tag{2.6}$$

The non-dimensional numbers in the above equations are defined as follows. Reynolds number, $Re = \frac{U_0 d_0}{\nu}$

Prandtl number, $Pr = \frac{\nu}{\kappa}$

Heat release number, $G = \frac{J}{\rho C_p} \frac{d_0}{U_0 T_0}$

From here on the asterisk on the non-dimensional terms will be dropped in this chapter for convenience.

2.4 Time Discretization

For time discretization we use Adams-Bashforth Crank-Nicolson semi-implicit scheme (Faure *et al.* (2008) and Armfield & Street (1999)). The non-linear advective term in the equation demand explicit treatment for which a second order accurate Adams-Bashforth scheme is used. The Crank-Nicolson scheme, which is implicit in nature, is used for the linear diffusion term. This scheme is unconditionally stable and improves the numerical stability of the overall time discretization. The pressure and buoyancy terms are treated implicitly. The method is illustrated below for computing u-velocity component at $(n+1)$th time step.

$$\frac{u^{n+1}-u^n}{\Delta t}+\big(\frac{3}{2}(\boldsymbol{u}.\nabla u)^n-\frac{1}{2}(\boldsymbol{u}.\nabla u)^{n-1}\big)=-\nabla p^{n+1}+\frac{1}{2Re}\big(\nabla^2 u^{n+1}+\nabla^2 u^n\big) \quad (2.7)$$

2.5 Method of Solution : Projection Method

In incompressible flows, the velocity and the pressure are coupled through the incompressibility constraint that leads to difficulty in the numerical simulation. In the late 1960's, Chorin (1968) and Temam (1969) introduced the concept of projection to solve the Navier-Stokes equations in primitive-variable form using the method of fractional step or operator splitting. The first step of the two-step method involves the calculation of the auxiliary velocity field $\hat{\boldsymbol{u}}$ using the Navier-Stokes equations in the absence of the pressure term. In the subsequent step a divergence-free velocity field is obtained by correcting the auxiliary velocity field using the updated pressure obtained from the Pressure Poisson equation (PPE). In the correction step, the initial velocity field is orthogonally projected to a non-divergent space such that the vorticity remains unchanged. The steps in the projection method can be

from the time discretized equation as follows.

$$\frac{\boldsymbol{u}^{n+1}-\boldsymbol{u}^{n}}{\Delta t}+(\boldsymbol{u}.\nabla\boldsymbol{u})^{n+\frac{1}{2}}=-\nabla p^{n+1}+\frac{1}{2Re}\big(\nabla^2\boldsymbol{u}^{n+1}+\nabla^2\boldsymbol{u}^{n}\big) \tag{2.8}$$

where $\boldsymbol{u}^n=\boldsymbol{u}(\boldsymbol{x},n\Delta t)$, $(\boldsymbol{u}.\nabla\boldsymbol{u})^{n+\frac{1}{2}}=(\frac{3}{2}(\boldsymbol{u}.\nabla\boldsymbol{u})^{n}-\frac{1}{2}(\boldsymbol{u}.\nabla\boldsymbol{u})^{n-1})$

Now writing the transient term on the LHS of Eq.2.8 as $\frac{(\boldsymbol{u}^{n+1}-\tilde{\boldsymbol{u}}^{n+1})+(\tilde{\boldsymbol{u}}^{n+1}-\boldsymbol{u}^{n})}{\Delta t}$, we can algebraically split the equation as:

$$\frac{\tilde{\boldsymbol{u}}^{n+1}-\boldsymbol{u}^{n}}{\Delta t}+(\boldsymbol{u}.\nabla\boldsymbol{u})^{n+\frac{1}{2}}=\frac{1}{2Re}\big(\nabla^2\boldsymbol{u}^{n+1}+\nabla^2\boldsymbol{u}^{n}\big) \tag{2.9}$$

$$\frac{\boldsymbol{u}^{n+1}-\tilde{\boldsymbol{u}}^{n+1}}{\Delta t}=-\nabla p^{n+1} \tag{2.10}$$

The viscous term in Eq. 2.9 contains $\boldsymbol{u}^{n+1}$ which can be replaced using Eq. 2.10. Rearranging the terms in the equation we get

$$\frac{\tilde{\boldsymbol{u}}^{n+1}-\boldsymbol{u}^{n}}{\Delta t}+(\boldsymbol{u}.\nabla\boldsymbol{u})^{n+\frac{1}{2}}=\frac{1}{2Re}\big(\nabla^2\tilde{\boldsymbol{u}}^{n+1}+\nabla^2\boldsymbol{u}^{n}\big)-\frac{\Delta t}{2Re}\nabla^2\nabla p \tag{2.11}$$

This can be rewritten as:

$$\frac{\tilde{\boldsymbol{u}}^{n+1}-\boldsymbol{u}^{n}}{\Delta t}+(\boldsymbol{u}.\nabla\boldsymbol{u})^{n+\frac{1}{2}}=\frac{1}{2Re}\big(\nabla^2\tilde{\boldsymbol{u}}^{n+1}+\nabla^2\boldsymbol{u}^{n}\big)-O(\Delta t^2) \tag{2.12}$$

Eqs. 2.12 and 2.10 are the two steps of the projection method due to Chorin. A lot of work has been done on this method in the past four decades to improve its accuracy, but it still remains a major area of research. Recently an overview on the projection method has been given by Guermond *et al.* (2006), discussing the current status and future challenges. The major issue is regarding the boundary condition for pressure. Chorin (1968) used a Neumann boundary condition for pressure, but this has been proved to lead to an O(1) error (Liu *et al.* (2004)).

In the present simulations we use a second-order incremental pressure-correction scheme proposed by Van Kan (1986). The first substep involves the calculation of velocity using the pressure gradient value from the previous time step. In the second substep the corrected velocity is obtained by introducing an auxiliary pressure which is obtained by solving the Poisson eqaution. The method is illustrated below for the equations discretized in time according to section 2.4.

$$\frac{\tilde{\boldsymbol{u}}^{n+1} - \boldsymbol{u}^n}{\Delta t} + (\boldsymbol{u}.\nabla\boldsymbol{u})^{n+\frac{1}{2}} = -\nabla p^n + \frac{1}{2Re}(\nabla^2\tilde{\boldsymbol{u}}^{n+1} + \nabla^2\boldsymbol{u}^n) \tag{2.13}$$

$$\frac{\boldsymbol{u}^{n+1} - \tilde{\boldsymbol{u}}^{n+1}}{\Delta t} = -\nabla\phi^{n+1} \tag{2.14}$$

where ϕ is defined as

$$\phi^{n+1} = p^{n+1} - p^n \tag{2.15}$$

and is obtained by solving the Poisson equation:

$$\nabla^2\phi^{n+1} = \frac{1}{\Delta t}\nabla.\tilde{\boldsymbol{u}}^{n+1} \tag{2.16}$$

2.6 Spatial Discretization

There are several methods such as finite difference, finite volume, spectral etc. to compute the spatial derivatives. As the geometry of the flow is simple we choose finite difference schemes for spatial discretization, as they are easy to implement. In 3D simulations the governing equations are solved in the cylindrical coordinate system, which restricts us to use second order central difference schemes to obtain the derivatives. For a uniformly spaced grid (shown in fig.2.2(a)) the finite

difference derivatives are obtained from the Taylor series expansion as follows.

$$\frac{\partial u}{\partial x} = \frac{u_{i+1} - u_{i-1}}{2\Delta x} \tag{2.17}$$

$$\frac{\partial^2 u}{\partial x^2} = \frac{u_{i+1} - 2u_i + u_{i-1}}{\Delta x^2} \tag{2.18}$$

In case of a non-uniform grid, the equations are transformed to a uniform grid in

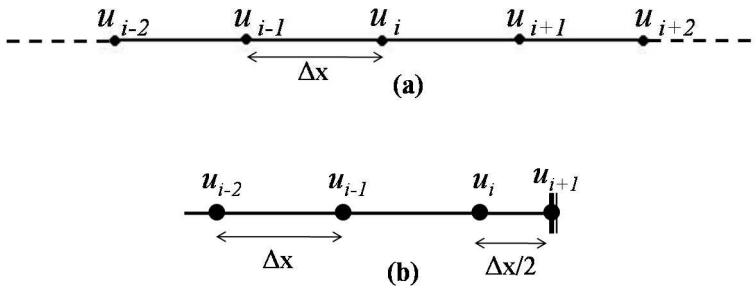

Figure 2.2: (a) One-dimensional uniform grid. (b) Grid with boundary point.

which the spatial derivatives are computed. Near the boundary (fig.2.2(b)) we use polynomial fitting of second order to compute the derivatives as

$$\frac{\partial u}{\partial x} = \frac{4u_{i+1} - 3u_i - u_{i-1}}{3\Delta x} \tag{2.19}$$

$$\frac{\partial^2 u}{\partial x^2} = \frac{2u_{i+1} - 3u_i + u_{i-1}}{0.75\Delta x^2} \tag{2.20}$$

2.7 Computational Grid

For spatial discretization of the equations we use a clustered cartesian grid for 2D simulations and a uniform cylindrical grid for 3D simulations. In both the cases, scalar quantities like pressure and temperature are computed at the cell centers

and velocity components at the center of corresponding cell faces. This type of arrangement is known as staggered grid or MAC mesh, which has been proposed by Harlow & Welch (1965). An advantage of using such a grid is that it prevents the pressure oscillations which are usually seen in finite difference solutions on a collocated grid (For detailed discussion see Patankar (1980)). Figure 2.3 illustrates the arrangement and index notation of flow variables in a 2D and 3D grid.

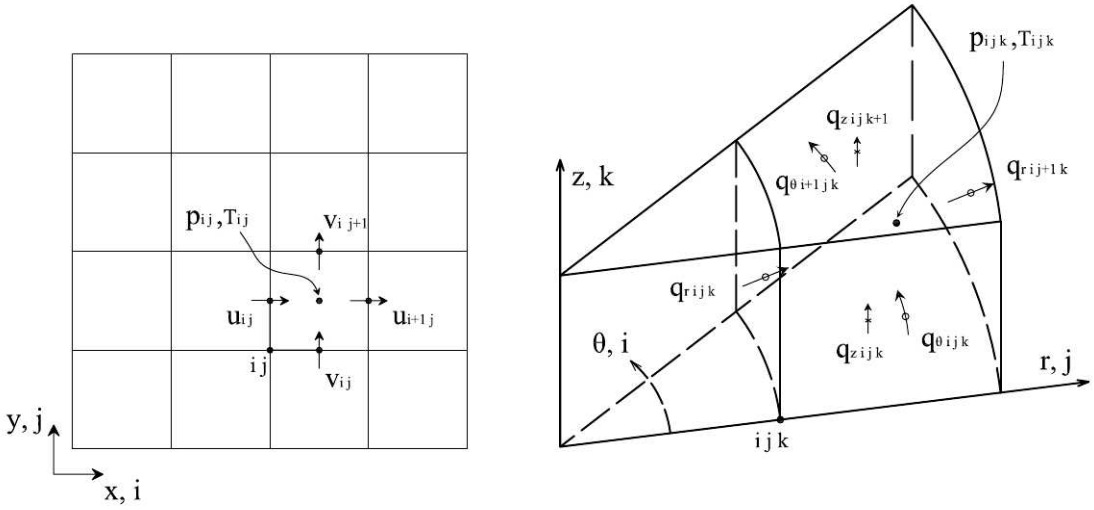

Figure 2.3: Staggered grid arrangement in 2D cartesian and 3D cylindrical coordinate systems.

In the 2D grid, the following clustering function is used.

$$x = x_{max}\frac{sinh(a\xi)}{sinh(a)}, \quad 0 \leq \xi \leq 1 \tag{2.21}$$

where x_{max} is the maximum length in the x-direction, a is the clustering parameter and ξ is the transformed coordinate.

2.8 Governing Equations : Revisited

2D Simulations

To solve the governing equations (2.4-2.6) in a 2D uniform grid, we transform the equations in the physical plane (non-uniform grid) to a uniform grid computational plane. The equations in the transformed plane are given in Eqs. 2.22-2.25. Here, u and v are the velocity components in x and y-directions respectively. ξ and η are the transformed coordinates corresponding to the x and y coordinates, which are related according to the clustering function in Eq. 2.21. We thus obtain

$$\xi_x \frac{\partial u}{\partial \xi} + \eta_y \frac{\partial v}{\partial \eta} = 0 \tag{2.22}$$

$$\frac{\partial u}{\partial t} + \xi_x u \frac{\partial u}{\partial \xi} + \eta_y v \frac{\partial u}{\partial \eta} = -\xi_x \frac{\partial p}{\partial \xi} + \frac{1}{Re}(\xi_{xx} \frac{\partial u}{\partial \xi} + {\xi_x}^2 \frac{\partial^2 u}{\partial \xi^2} + \eta_{yy} \frac{\partial u}{\partial \eta} + {\eta_y}^2 \frac{\partial^2 u}{\partial \eta^2}) \tag{2.23}$$

$$\frac{\partial v}{\partial t} + \xi_x u \frac{\partial v}{\partial \xi} + \eta_y v \frac{\partial v}{\partial \eta} = -\eta_y \frac{\partial p}{\partial \eta} + \frac{1}{Re}(\xi_{xx} \frac{\partial v}{\partial \xi} + {\xi_x}^2 \frac{\partial^2 v}{\partial \xi^2} + \eta_{yy} \frac{\partial v}{\partial \eta} + {\eta_y}^2 \frac{\partial^2 v}{\partial \eta^2}) \tag{2.24}$$

$$\frac{\partial T}{\partial t} + \xi_x u \frac{\partial T}{\partial \xi} + \eta_y v \frac{\partial T}{\partial \eta} = \frac{1}{RePr}(\xi_{xx} \frac{\partial T}{\partial \xi} + {\xi_x}^2 \frac{\partial^2 T}{\partial \xi^2} + \eta_{yy} \frac{\partial T}{\partial \eta} + {\eta_y}^2 \frac{\partial^2 T}{\partial \eta^2}) \tag{2.25}$$

3D Simulations

The major difficulty in solving the governing equations in cylindrical coordinates is due to the geometric singularity at $r = 0$. This problem has been addressed by Verzicco & Orlandi (1996). They use a staggered grid and rewrite the terms in the equations in terms of $q_\theta = u_\theta$, $q_r = r.u_r$ and $q_z = u_z$ (see Eqs. 2.26-2.29), which avoids the computation of flow variable at $r = 0$.

$$\frac{\partial q_r}{\partial r} + \frac{\partial q_\theta}{\partial \theta} + r \frac{\partial q_z}{\partial z} = 0 \tag{2.26}$$

$$\frac{D q_\theta}{D t} = -\frac{1}{r}\frac{\partial p}{\partial \theta} + \frac{1}{Re}\left[\frac{1}{r}\left(\frac{\partial}{\partial r} r \frac{\partial q_\theta}{\partial r}\right) - \frac{q_\theta}{r^2} + \frac{1}{r^2}\frac{\partial^2 q_\theta}{\partial \theta^2} + \frac{\partial^2 q_\theta}{\partial z^2} + \frac{2}{r^3}\frac{\partial q_r}{\partial \theta}\right] \tag{2.27}$$

$$\frac{Dq_r}{Dt} = -r\frac{\partial p}{\partial r} + \frac{1}{Re}\left[r\frac{\partial}{\partial r}\left(\frac{1}{r}\frac{\partial q_r}{\partial r}\right) + \frac{1}{r^2}\frac{\partial^2 q_r}{\partial \theta^2} + \frac{\partial^2 q_r}{\partial z^2} - \frac{2}{r}\frac{\partial q_\theta}{\partial \theta}\right] \tag{2.28}$$

$$\frac{Dq_z}{Dt} = -\frac{\partial p}{\partial z} + \frac{1}{Re}\left[\frac{1}{r}\frac{\partial}{\partial r}\left(r\frac{\partial q_z}{\partial r}\right) + \frac{1}{r^2}\frac{\partial^2 q_z}{\partial \theta^2} + \frac{\partial^2 q_z}{\partial z^2}\right] \tag{2.29}$$

The terms on the left hand side of the above equations are total derivates. A detailed procedure of implementation that includes obtaining derivatives near $r = 0$ has been discussed in Verzicco & Orlandi (1996).

2.9 Solution of Linear Algebraic System of Equations

In our simulations, the Crank-Nicolson scheme has been used for time discretization of the viscous terms. This is implicit in nature and leads to a system of linear algebraic equations that needs to be solved. A similar situation is also encountered while obtaining the pressure field from PPE. For solving these systems of equations we use the Successive Over-Relaxation (SOR) method, which is an indirect or iterative procedure. This method is simple to implement and can be parallelized easily.

2.10 Code Parallelization

The Direct Numerical Simulation of unsteady incompressible Navier-Stokes equations is computationally intensive and demands large CPU time and physical memory (RAM). The calculation of the flow field at a particular time step using the projection method involves solving the Pressure Poisson Equation which is an elliptic Partial Differential Equation (PDE). It is well known that elliptic PDEs have

a slow rate of convergence and hence for major share of computational time. According to our experience, 2D simulations can be done using a serial code (which is run only on one processor) at high resolution also, typically taking a couple of days to solve. In case of 3D simulations, it is not practical to use a serial code even at lower resolutions as it takes several weeks to compute. This compels us to parallelize the code and run it on multiple processors simultaneously.
The architecture of a parallel computer plays a major role in arriving at suitable programming methods and algorithms. Based on the memory system the parallel architecture is classified into the following.

- Shared Memory - All processors operate independently, but share the same memory resources.
- Distributed Memory - Each processor operates independently and has its own local memory.
- Hybrid Distributed-Shared Memory - A combination of the above architectures.

Programming on a shared memory computer is much easier as compared to others. In the present market these computers can have a maximum of 16 processors. This solves the computing-time issue to a certain extent, but becomes impractical for high resolution simulations. On the other hand, there is no restriction on the number of processors that a distributed memory computer can have. This motivates us to parallelize the DNS code based on distributed memory using Message Passing Interface (MPI), a language-independent communications protocol used to program parallel computers (Wikipedia). A schematic of the distributed memory architecture is shown in figure 2.4.

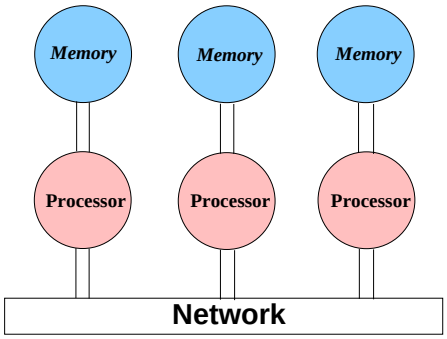

Figure 2.4: A schematic of distributed memory architecture.

As the DNS calculations are carried out on a grid, we choose domain decomposition technique for parallelizing the code. The basic idea here is to divide the grid into several sub-domains and compute the flow variables in these sub-domains on different processors. A row/column of ghost cells are provided at the boundary of each sub-domain to hold the values communicated from neighbouring processors. A novel parallel algorithm which uses minimal physical memory and data communication has been designed. The major steps involved are the following.

- Dividing the computational grid into several sub-domains and distributing them to different processors.
- Gathering of flow field data from each processor to print them into output files.
- A synchronized communication of sub-domain boundary values between neighbouring processors when they get updated.

In the first attempt, we decomposed the domain only in one dimension. This involves slicing of cylindrical grid into sub-domain normal to the z-direction. The number of processors is chosen in such a way that equal sized sub-domain are

obtained. The 1D decomposition of the domain is fairly straight forward to implement, but restricts the usage of maximum number of processors to the number of grid points in z-direction. A diagram illustrating the decomposition and communication of boundary values between neighbouring sub-domains is shown in figure 2.5.

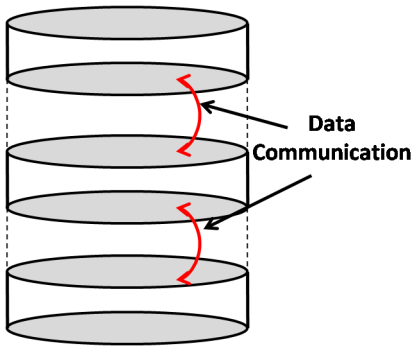

Figure 2.5: A schematic of 1D domain decomposition in r-z plane.

Domain decomposition in two dimensions has been done in the r-z plane. The computational grid is sliced along both r and z-directions resulting in disk or donut shaped sub-domains. Figure 2.6 shows the schematic of the decomposition in r-z plane. Here the processors are arranged in a 2D array such that the number of processors along a particular dimension is equal to the number of sub-domains in that dimension. If the number of sub-domains along r-direction and z-direction are jp and kp, then the total number of processors (np) required for the simulation is given by $np = jp \times kp$. Parallelization of the code in two dimensions is not as easy as in one dimension and needs utmost care to synchronize the data communication, which otherwise leads to deadlocks in the program; the communications involved are shown in figure 2.6. In principle the number of processors that can be used

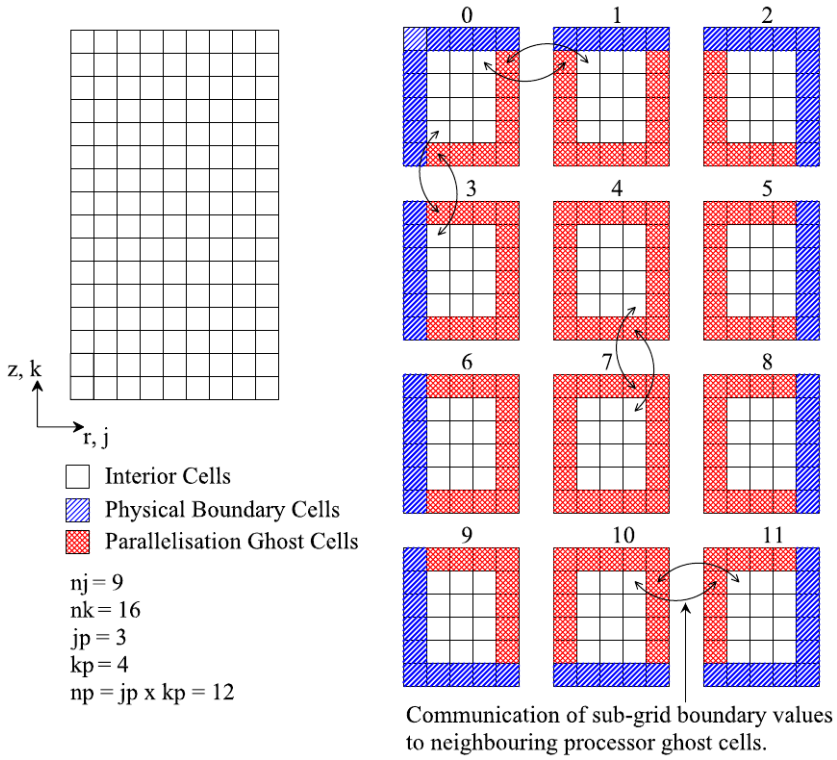

Figure 2.6: A schematic of 2D domain decomposition in r-z plane.

here is much more than in 1D decomposition. As an example, for a $100 \times 100 \times 100$ grid the program allows us to use 10000 processors, which of course might not be the most efficient configuration. The code is written in such a way that a shared memory programming can be done in the θ-direction, thereby making the program highly efficient to run on hybrid memory super-computers.

The code has been initially written and tested on a DELL T7400 work-station which has 8 processors. The final computations have been be done on the Tata's super-computer Eka at Computational Research Laboratories, Pune.

CHAPTER 3

TWO-DIMENSIONAL SIMULATIONS

We start with two-dimensional (2D) simulations in an attempt to explore different computational procedures, solution algorithms, numerical schemes and boundary conditions. Sreenivas (2004) has discussed that the effect of volumetric off-source heating on entrainment is a 2D process where the axial stretching of the flow occurs due to acceleration of the fluid. Moreover, the study of a 2D starting plume could be relevant for flow in line or row clouds. Much work on a plume originating from a point source in an infinite domain has been reported in the literature (Fuji (1963) and Gebhart (1973)). However, we are not aware of any results on plumes rising from a finite heat source on a solid wall for the validation of our DNS code. Therefore we verify the code by satisfying conservation principles like the divergence-free condition and the conservation of buoyancy flux. In this chapter, we first present the solutions for an unheated plume in laminar and turbulent regimes and later move onto heated plume to study the effects of off-source heating.

3.1 Simulation Details

As discussed in chapter 2, a non-uniform Cartesian grid used in the simulation is clustered near the bottom wall and the center-line (figure 3.1). Simulations have been done for different values of the various parameters which are tabulated in table 3.1. The results presented here are computed using a grid resolution of 256 x 256, in a domain of size $80d_0$ along both horizontal and vertical directions. Laminar flow is computed for the Reynolds number of 100 and turbulent flow for 3000. The

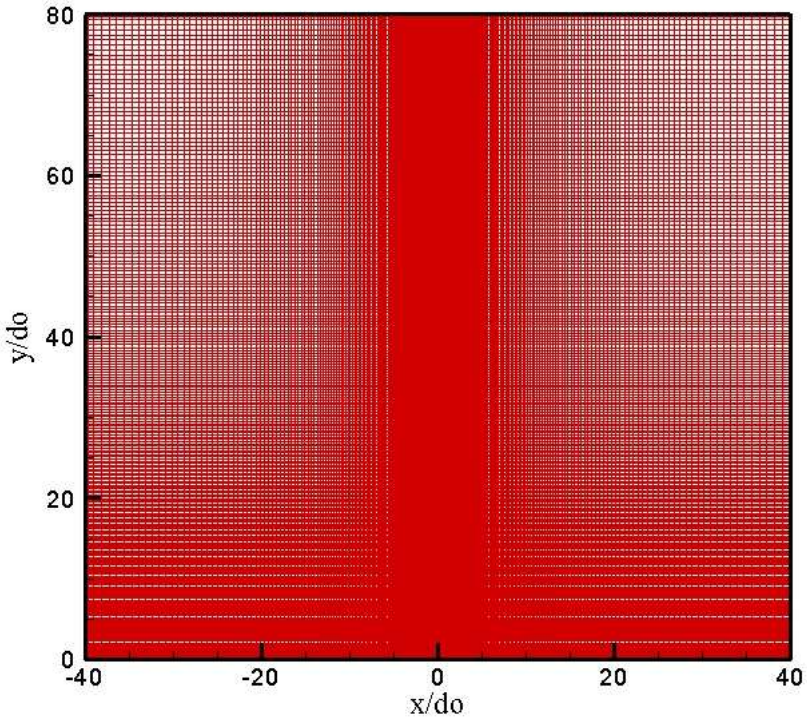

Figure 3.1: Computational grid used in simulations (resolution : 256×256).

Simulation Parameters	**Values**
Domain size	$40d_0$ x $40d_0$, $80d_0$ x $80d_0$
Grid resolution	64 x 64, 128 x 128, 256 x 256
Time step size	0.001, 0.005, 0.01
Reynolds Number	100, 1000, 3000

Table 3.1: The values of Simulation Parameters used in simulation.

value of the Prandtl number is 1 in both cases.

3.2 Boundary Conditions

One of the major difficulties in the simulation of a plume is due to the lateral and outflow boundary conditions, as there are no clear physical boundaries. The bottom boundary is a solid wall with a heat source at the center, which imposes a no-slip and no-flow through condition. Our study is a class of free shear flows where there is significant entrainment of the ambient fluid through the edges. In the literature, free-slip and traction-free conditions have been used at the lateral boundary Boersma *et al.* (1998). The free-slip condition does not allow flow through the boundary,which may affect the entrainment. The traction-free condition permits flow across the lateral boundary and also satisfies the condition that the entrainment velocity reaches a constant value asymptotically. Hence, we use the traction-free conditions at the lateral boundary. The selection of outflow boundary is crucial, as the use of an inappropriate condition will lead to spurious reflection in the flow from the outflow. We have carried out numerical experiments with convective boundary condition and Zero Normal Derivative (ZND) of flow variables at the outflow, and found ZND to be more appropriate.

3.3 Laminar Flow - Code Verification

Figure 3.2 show the vorticity contours and velocity vector plots for the laminar starting plume. The flow begins with the formation of a pair of counter-rotating vortices near the heat source (figure 3.2(a)). These vortices, which constitute the plume-head, ascend vertically, attached to the core flow. As the flow is incompressible, the divergence of the velocity vector provides a measure for the accuracy of the present code. In our simulations the divergence free condition is satisfied to an order of 10^{-6}. Another quantity which is conserved along the streamwise direction in a fully developed laminar plume is the Buoyancy Flux Integral (BFI) defined as

$$BFI = \frac{\int T v dx}{T_0 U_0 d_0} \tag{3.1}$$

in non-dimensional form. The peaks in the BFI plot (figure 3.3) correspond to the position of the plume head at that particular time. Once the plume head goes out of the domain, BFI remains nearly constant along the streamwise direction. The centerline velocity plotted along the streamwise direction is shown in figure 3.3.

3.4 Turbulent Flow - Code Verification

A similar procedure as used in the computation of a laminar plume has been adopted for verification of the code for the turbulent plume. The incompressibility condition is again satisfied to an order of 10^{-6}. The BFI fluctuates significantly along the streamwise coordinate at all the times (figure 3.4). It can be observed that all the fluctuations are about a constant mean value which is shown by a broken-line in the figure. We cannot average the flow quantities in time, as we are looking at a starting plume where the height of the plume changes at every instant.

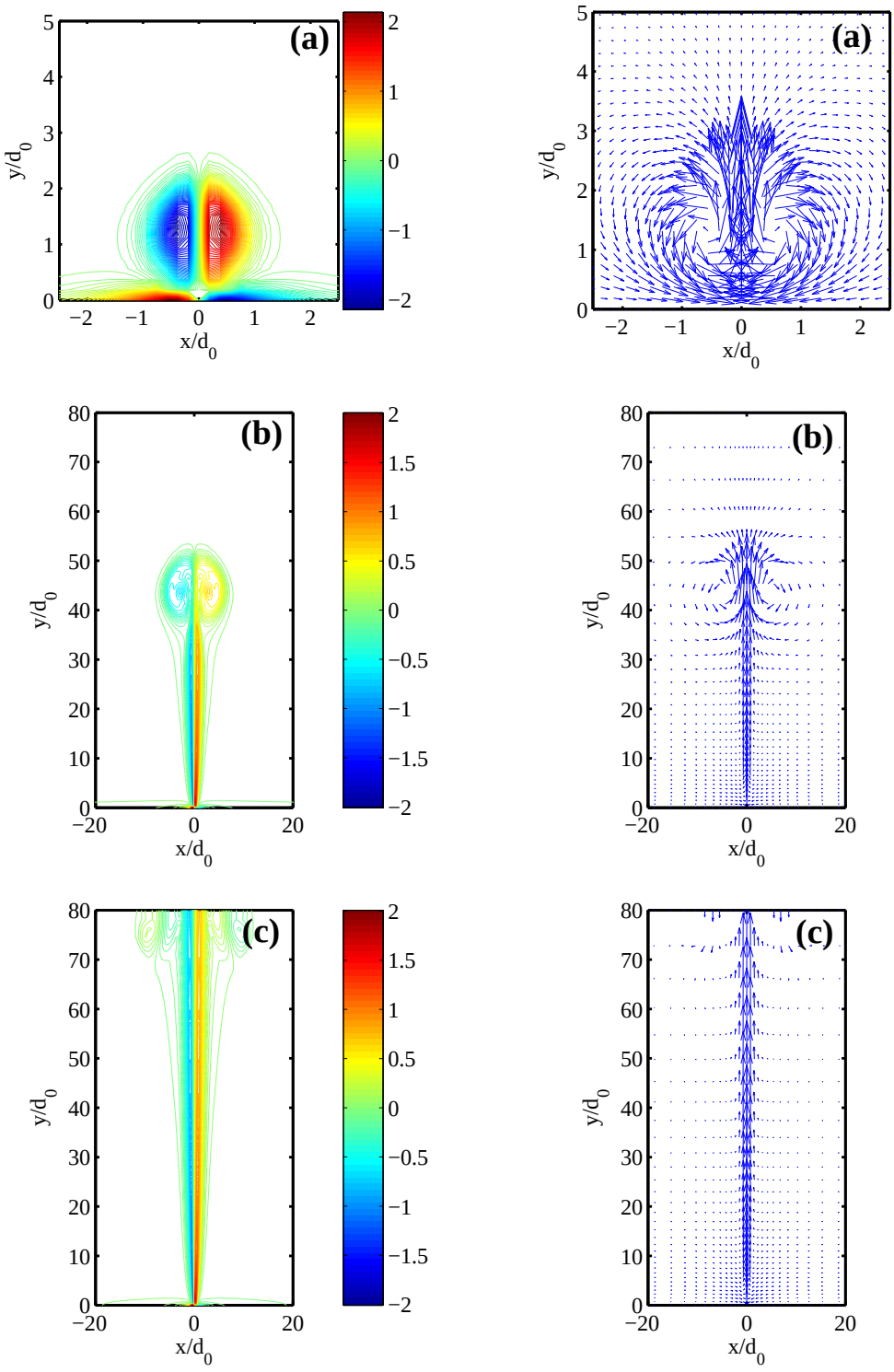

Figure 3.2: Vorticity contours and velocity vector plots of the laminar plume at different non-dimensional time instants. (a) $t^* = 10$, (b) $t^* = 100$, (c) $t^* = 200$

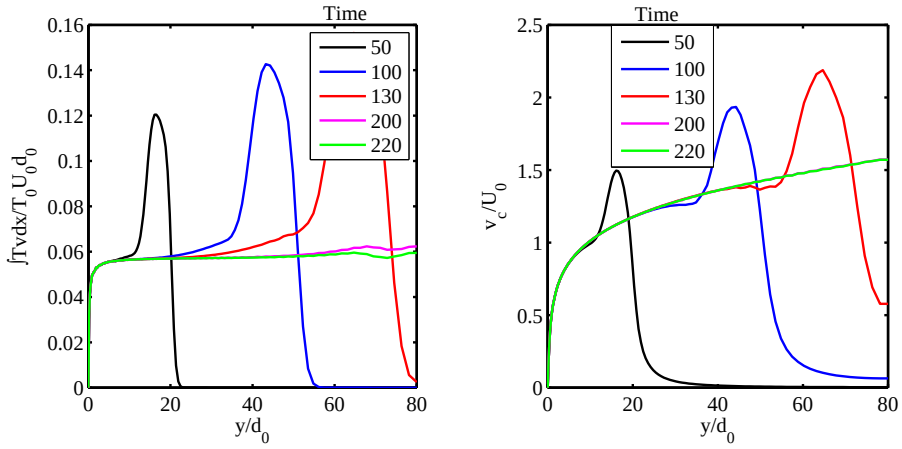

Figure 3.3: Plots of buoyancy flux integral and centerline velocity along streamwise coordinate at different times.

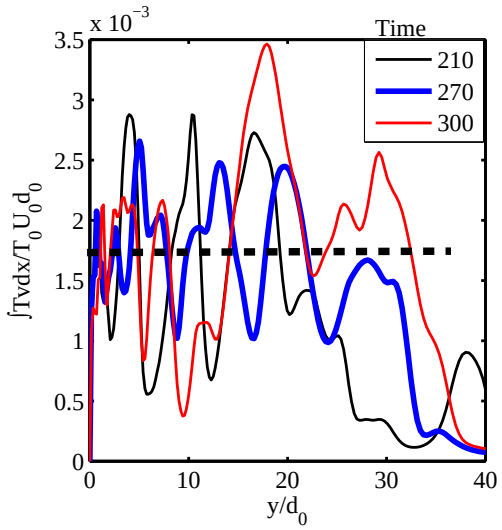

Figure 3.4: Plots of buoyancy flux integral and centerline velocity along streamwise coordinate at different times.

3.5 Classical Turbulent Starting Plume

The evolution of an unheated turbulent plume at a Reynold number of 3000 is shown in figure 3.5. In order to have an early transition, the flow is tripped by adding 5% noise (with zero mean) to the heat source temperature T_0. It can be seen that the plume spreads at a nearly constant rate and has developed a sinuous instability. One interesting observation about the turbulent starting plume is that the plume head detaches from the core flow. Futhermore, it remains in a laminar state and rises with greater vertical velocity than the core flow.

3.6 Starting Plume with Off-Source Heating

In this section, we look at a starting plume subjected to off-source heating, which is dynamically similar to the latent heat released due to condensation of water vapour in the clouds. The volumetric heating starts when the plume head reaches the heat-injection zone (HIZ) located between y/d_0 of 15 and 35. The amount of heat added in HIZ corresponds to a non-dimensional heat release number (G, defined in chapter 2) of 0.01 and is distributed across the flow according to a Gaussian profile with a width determined from the velocity distribution of the unheated plume solution.

Figure 3.6 illustrates the flow structure of a heated plume at different times. Off-source heating imparts an additional buoyancy to the fluid that accelerates the plume as it reaches HIZ. The spread rate of the plume is seen to decline in HIZ, and as the plume passes beyond HIZ it increases considerably. It is also evident that because of the off-source heating the entrainment velocity (cross-stream velocity near the lateral boundary) is significantly lower as compared to that in the pre-HIZ region (see figure 3.7). The recovery of spread rate above the HIZ can be attributed to relaxation towards the growth rate characteristic of an unheated

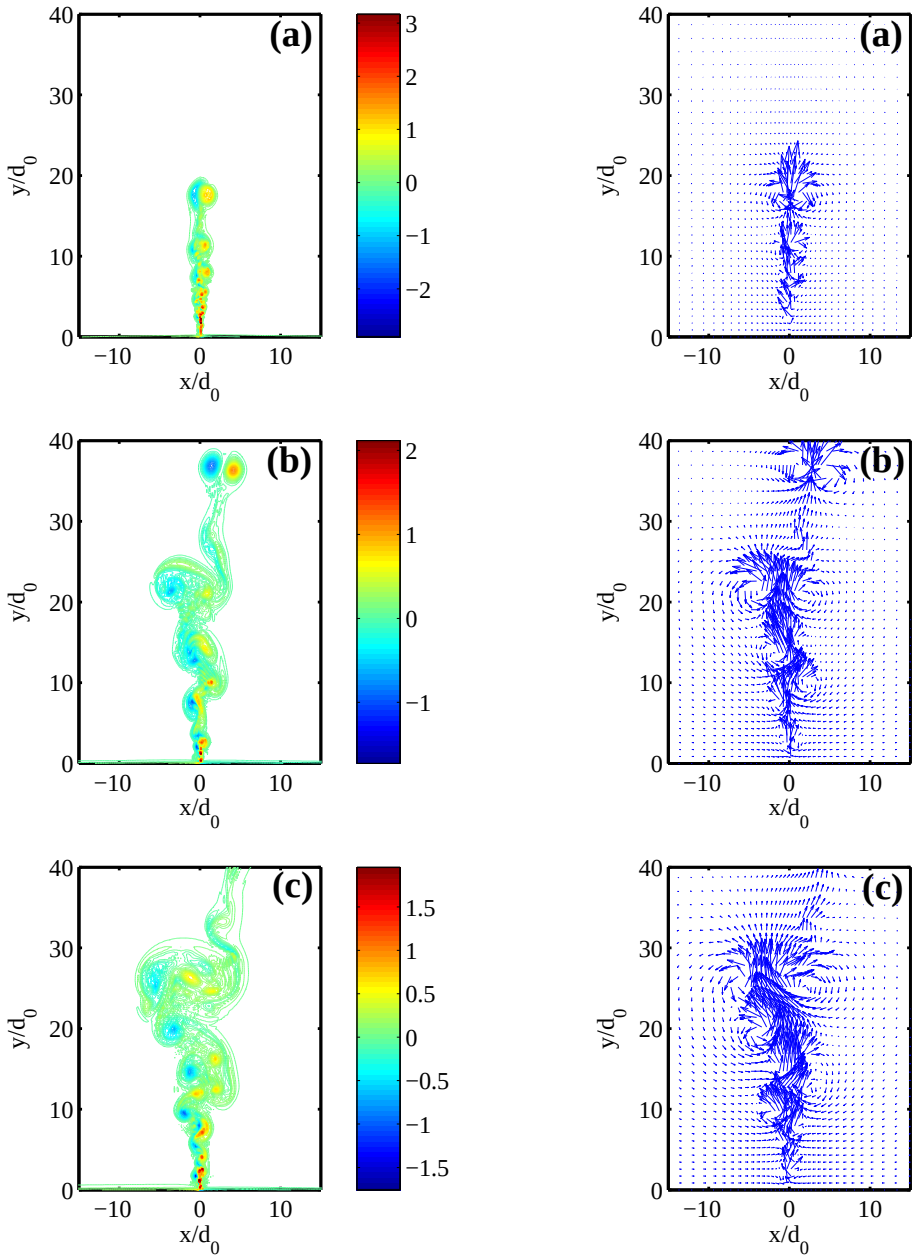

Figure 3.5: Vorticity contours and velocity vector plots of the turbulent plume at different non-dimensional time instants. (a) $t^* = 100$, (b) $t^* = 200$, (c) $t^* = 250$

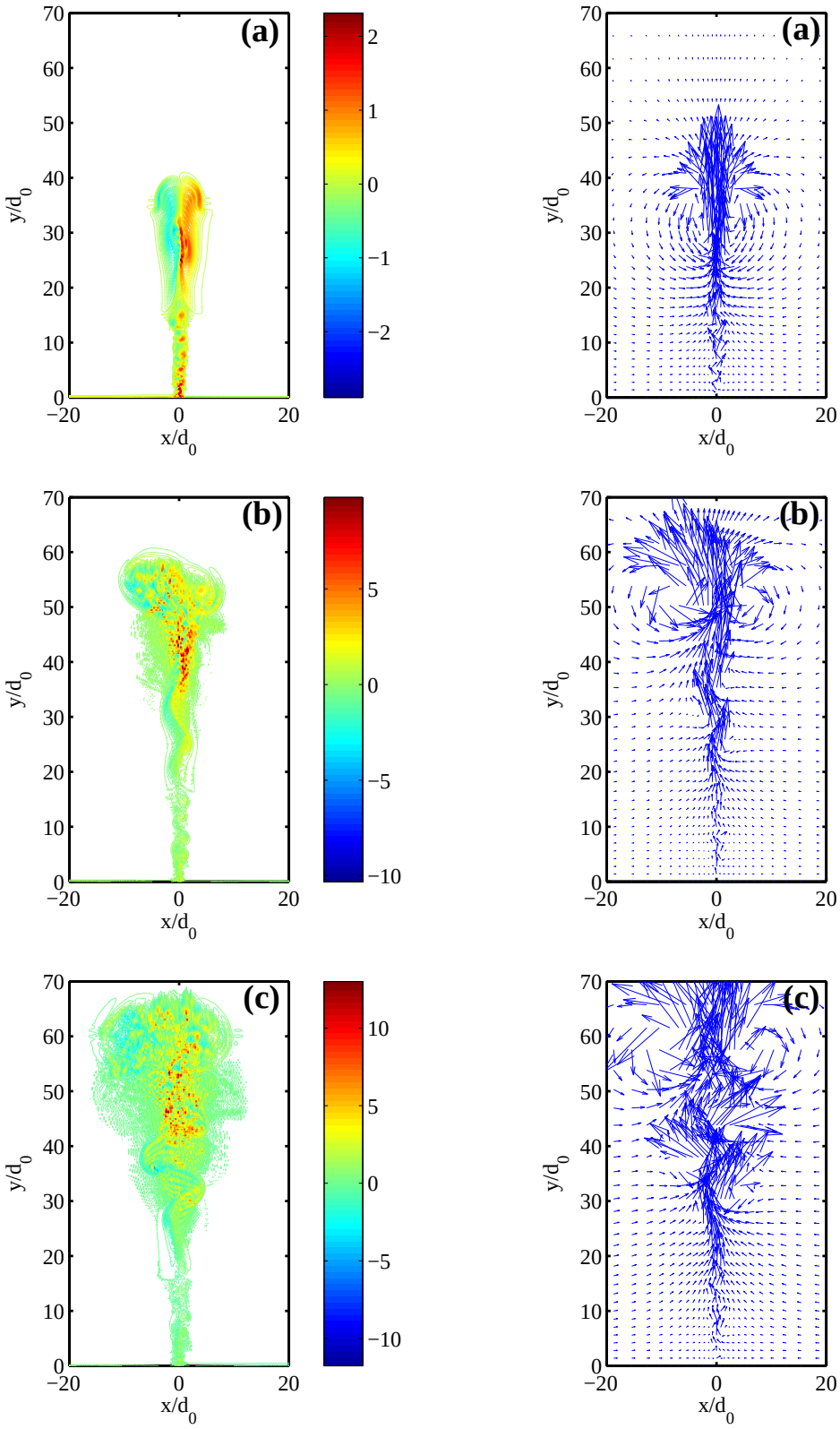

Figure 3.6: Vorticity contours and velocity vector plots of the turbulent start plume with off-source heat addition. $Re = 3000$, $G = 0.01$ (a) $t^* = 100$, (b) $t^* = 200$, (c) $t^* = 250$

turbulent plume.

A comparison of vorticity contours for an unheated and heated starting plume is shown in figure 3.8. The coherent structures which are distinctly seen in the unheated plume are disrupted due to off-source heating. The heating also has an effect in enhancing the vorticity values in the flow. The maximum vorticity in the heated case is found to be 5 times greater than that in unheated case. Furthermore, with the heated plume, we observe a protected core with diffuse boundaries, which is consistent with the experimental findings of Venkatakrishnan *et al.* (1999).

The results indicate that even a 2D simulation can capture the reduction in entrainment due to off-source heating, which is in agreement with entrainment reduction due to the axial stretching and subsequent stabilization of shear layer as suggested by Sreenivas & Prasad (2000) and Sreenivas (2004). This model is predominantly based on a 2D process, thus it can be captured by the present 2D simulations.

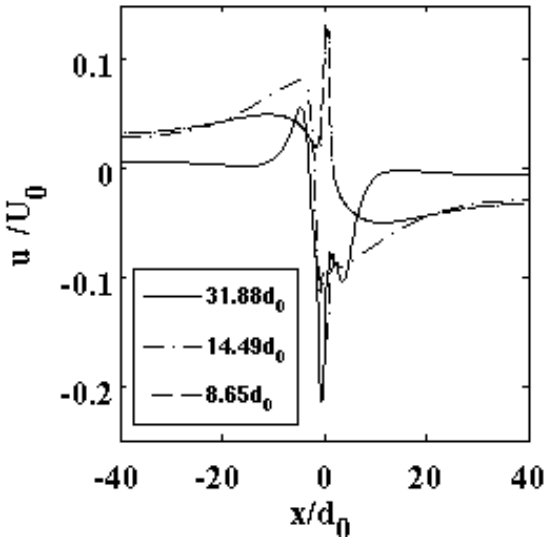

Figure 3.7: Horizontal velocity variation normal to the core flow in the plume, indicating entrainment velocity at different streamwise coordinates. The continuous line in the plot is at a height in HIZ towards the top.

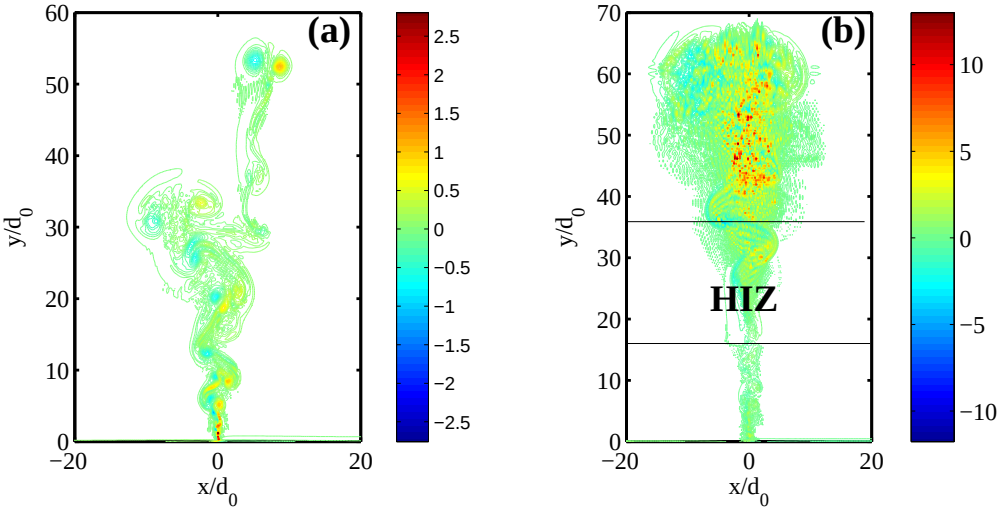

Figure 3.8: Vorticity contours of an unheated and a heated starting plume at a $Re = 3000$. (a) $G = 0$, $t^* = 310$, (b) $G = 0.01$, $t^* = 150$

CHAPTER 4

THREE-DIMENSIONAL SIMULATIONS

The results of 2D simulations show promise and reproduce the major features that have been observed in earlier experiments on jets and plumes with off-source heating. The 2D simulations can not however capture all aspects of three-dimensional (3D) turbulent flows, as the vortex stretching and tilting mechanisms are absent. So it is necessary to carry out 3D simulations to capture the characteristics of the real flow. This chapter presents results of 3D starting plumes with and without off-source heating.

4.1 Boundary Conditions

The bottom and top boundary conditions are no-slip and zero-normal derivative respectively, the same as in the 2D simulations. In the case of axisymmetric flow the use of the traction-free condition at the lateral boundary will reduce to the condition $\frac{\partial u_r}{\partial r} \rightarrow 0$. This implies that if u_r tends to a non-zero constant as $r \rightarrow \infty$, the inflow from the ambient will in general be infinite, which is not acceptable. According to Schneider (1981), for a sufficiently high Reynold number (≥ 500) the outer flow, and therefore also the flow at a lateral boundary sufficiently far from the core flow, is irrotational. Therefore, we shall take the lateral boundary conditions to be (a) $\frac{\partial r u_r}{\partial r} = 0$ (so the mass influx from the ambient, proportional to $r u_r$, is finite), and (b) $\omega = 0$ (the vorticity is zero as the flow is irrotational).

Simulation Parameters	**Values**
Grid resolution	$80d_0 \times 80d_0 \times 80d_0$, $100d_0 \times 100d_0 \times 100d_0$, $128d_0 \times 128d_0 \times 128_0$, $256d_0 \times 256d_0 \times 256d_0$
Time step size	0.001, 0.005, 0.01
Reynolds Number	100, 1000, 2000, 3000

Table 4.1: The values of Simulation Parameters used in the computations.

4.2 Simulation Details

In the 3D simulations, we initially used a rectangular domain to solve the governing equations. This demanded a high resolution grid in order to capture the axisymmetry of the off-source heating. This problem was resolved by using a cylindrical domain in all our computations. The governing equations are singular at the axis $r = 0$, which we handle using a method proposed by Verzicco & Orlandi (1996) (see section 2.8). As the simulations are computationally intensive, the code has been parallelized using the domain decomposition method. The final computations have been carried out on the super-computer *Eka* at the Tata Computational Research Laboratories, Pune, India.

Simulations have been carried out for different values of the various parameters listed in table 4.1. The results presented here are computed using a grid resolution of $100 \times 100 \times 100$, in a domain of size $15d_0$ in the streamwise direction and $12d_0$ in the radial direction. Laminar flow is computed for the Reynolds number (defined in section 2.3) of 100 and turbulent flow for 2000. The value of the Prandtl number is taken as 1 in both cases.

In the case of turbulent flow simulations, we trip the flow by adding synthetic white noise (around 5%) to the heat source temperature (T_0) at around 40 randomly chosen meshes. As the the elements in a cylindrical grid do not all have the same area, the tripping method makes sure that the mean of the area-weighted values of

the imposed disturbance levels is zero.

4.3 Laminar Flow - Validation

The contours of vertical velocity at different times for the laminar axisymmetric starting plume are shown in figure 4.1. The development of the plume is seen to be qualitatively similar to that in 2D simulations. Here, the plume head is a vortex ring which is formed near the heat source as the flow starts. As the plume-head moves out of the computational domain, the flow within the domain eventually tends towards a self-similar state.

For the verification of the code, we follow the same procedure as in 2D simulations. The divergence-free condition is satisfied to an order of 10^{-8}. Figure 4.2 shows the buoyancy flux integral (BFI) plotted along the streamwise direction at different instant of time. The peaks in the graph correspond to the position of the plume-head; as the plume reaches a self-similar state, the BFI tends to remains nearly constant on an average. The self-similar velocity profile obtained from the present simulations has been compared with the analytical expression given in Yih & Wu (1981) and is found to be in good agreement with it (figure 4.3).

4.4 Turbulent Flow - Verification

The variation of BFI along the streamwise coordinate is shown is figure 4.4. Even though the BFI values fluctuate as expected in turbulent plumes, an approximate mean line can be visually constructed (broken line in the figure), indicating that the mean BFI is constant over time well upstream of the plume-head. Furthermore, the incompressibility condition is satisfied to an order of 10^{-7}. These serve as

consistency tests for the present 3D turbulent code.

4.5 Turbulent Starting Plume with and without Off-Source Heating: Non-dimensional Parameters

In this section, we present the results of 3D turbulent simulations and discuss the effects of off-source volumetric heating on the dynamics of the starting plume. The off-source heat-injection zone (HIZ) is between the heights $z_b = 7d_0$ and $z_t = 10d_0$. The heating begins when the plume-head reaches the bottom of the HIZ and a constant amount of heat per unit volume per unit time (J) is added across the plume. A threshold on the temperature value ($0.001T_0$ in the present case) is used to determine the plume width for heat injection, making use of the fact that the temperature of the plume fluid will be greater than that of the ambient fluid.

The other non-dimensional number relevant to the flow is the bulk Richardson number (Ri), defined as

$$Ri = \frac{\triangle \rho g b}{\rho U^2},$$

where $\triangle\rho$ is the (local) change in the density of the fluid, b the local characteristic length and U the local characteristic velocity. This can be reduced to the non-dimensional flow variable as

$$Ri = \frac{\triangle T}{T} \frac{b}{d_o} \left(\frac{U_o}{U}\right)^2$$

In clouds, the value of the local Richardson number Ri varies from 0.1 to 2 in the cumulus type and from 0.3 to 3 in the cumulonimbus type clouds Venkatakrishnan *et al.* (1999). In order to obtain the Richardson number in our simulation, the relation

Heat release number(G)	**Richardson number**(Ri)
0.01	0.06
0.05	0.3
0.1	0.6

Table 4.2: Non-dimensional heat release numbers and the corresponding Richardson numbers used in computations.

$$Ri = G\left(\frac{b}{d_0}\right)^2\left(\frac{U_0}{U}\right)^3$$

is used in terms of the non-dimensional heat release number (G) and the values are tabulated in table 4.2.

4.6 Results

We present here a quick look summary of the observations that follow from the 3D starting plume simulations reported in this thesis. For this purpose we chiefly look at axial section of the azimuthal and axial components of the velocity and the vorticity vector fields in sections 4.6.1 and 4.6.2, and the temporal evolution of the axial distribution of the velocity and vorticity components in section 4.6.3.

4.6.1 Velocity Plots

Figure 4.5 and 4.6 show visualizations of the fluctuating turbulent velocity field with different colours representing ranges in the visualized variable. Contours of u_θ for four different levels of volumetric heating ($G = 0, 0.01, 0.05$ and 0.1), at time $t^* = 28$ in $\theta = 0,\pi$ plane (or the $x = 0$ plane) are shown in figure 4.5. At the two lowest values of heating the velocity fields are largely similar. For $G = 0.05$, the plume-head appears to have virtually separated away from the rest of the plume, leaving a region within the heat-injection zone (HIZ) where the velocity values are

very low. At this value of the heating the plume-head is just crossing the upper boundary of HIZ. When the heating is further increased to $G = 0.1$, the plume-head has crossed the upper boundary of HIZ. The velocity field within the HIZ still shows only very low values, although there are streak structures just above the lower boundary of HIZ. It can be noted that the width of the plume-head is appreciably narrower (about a third) when compared to the width of the unheated plume just below the beginning of the HIZ.

Figure 4.6 shows the azimuthal velocity field, at the last time step where computations were terminated. The times at which the computation was terminated are noted in each diagram. For $G = 0$ and $t^* = 35$, the unheated plume has just reached the top of the heat-injection zone. At $G = 0.01$ the plume head has crossed the upper boundary of HIZ and the width of the plume within HIZ is slightly lower than that of the unheated plume. On the whole the red and green regions within the heat injection zone are now more elongated than in the unheated case, consistent with the acceleration that the fluid experiences due to the additional buoyancy force in the HIZ. At $G = 0.05$ and $t^* = 31$ the plume-head has gone beyond the top of the HIZ (compare with figure 4.5 at $G = 0.05$) and is followed by a region in the upper half of HIZ where the velocity remains low. Also, compared to the flow at $t^* = 28$, an appreciable velocity field has emerged in the lower half of HIZ. In the case of $G = 0.1$, the computation has been terminated at $t^* = 28$, at the same instant at which the flow is shown in figure 4.5. Comparing the two flows shown here, at $G = 0.05$ and $G = 0.1$ (although at different times), we see that increase in heating has resulted in a narrowing of the plume-head (almost by a factor of half).

A similar visualization of the streamwise velocity field is shown in figure 4.7. Comparing the data at $G = 0$ and $G = 0.01$, we once again see that a narrow

plume-head is emerging from the top of HIZ. The width of the plume within HIZ is slightly greater at the bottom of HIZ and slightly narrower at the top. At $G = 0.05$, $t^* = 31$ there is a relatively high velocity at and beyond the top of HIZ due to the additional buoyancy generated by the off-source heating. Although the core here remains relatively narrow, there is a wider region of low values of the u_z field at the top of HIZ. Even in the case of $G = 0.1$ and $t^* = 28$, there is a larger region of low velocity fluid outside the core of high velocity fluid in the top half of HIZ. It must be noted that in the colour code adopted for the velocity field, the green regions represent relatively low values of the globally normalized velocity $\frac{u_z}{U_o}$. It is therefore necessary to point out that the wider regions seen in HIZ at $G = 0.05$ and 0.1 also represent regions where the velocity, as a fraction of the (generally higher) center-line velocity, is lower than in the unheated plume. More detailed analyses of figures 4.6 and 4.7 are necessary to understand the precise nature of the changes in the velocity profiles across the plume. It is worth noting that the characters of the distribution of u_θ and u_z are very different. In particular, it should be remembered that figure 4.7 displays the values of the instantaneous streamwise velocity rather than a turbulent fluctuating component, which is usually obtained by subtracting an appropriately defined mean value. Such a mean value is difficult to define in the non-stationary turbulent flow of the starting plume that we are studying here, except in the case of the azimuthal field where the mean is zero by symmetry. This has an important implication for the interpretation of these pictures, where the azimuthal velocity field represents the turbulent fluctuations and the axial field does not. The axial field represents the value of the total velocity, in which the turbulent component is not in general a very large part.

4.6.2 Vorticity Plots

The contours of the azimuthal vorticity (ω_θ) field are shown in figures 4.8 and 4.9. Note that unlike the azimuthal velocity u_θ, the ω_θ field here represents the total azimuthal vorticity. We see that the injection of heat has an appreciable influence on the vorticity field at $G = 0.05$ and 0.1, and the plume-head takes the rough shape of an arrow head. Interestingly, towards the bottom of the arrow head the vorticity values near the axis are extremely low. It appears therefore as if vorticity is concentrated in the region near the tip of the arrow head. Once again with these diagrams the width of the plume appears larger in the heat-injection zone with the addition of heat.

Figure 4.9 shows the same field at different times, each marking the termination of the computer run at the respective heating levels. By and large the conclusions are similar. At $G = 0.05$ and $t^* = 31$ the plume head has penetrated well above HIZ. In case of $G = 0.1$ and $t^* = 28$, we also see a tendency for the plume head like structure to separate from the rest of the plume, corresponding perhaps to a puffing regime of the kind also seen in Figure 4.6. Note in particular the fibrous streaks which are below the plume-head towards the bottom of the heat injection zone.

The streamwise vorticity at $t^* = 28$ is plotted in figure 4.11. At $G = 0.01$ it can be seen that the vortex patches are stretched presumably due to acceleration resulting from the additional buoyancy force in HIZ. (This can be seen clearly even in the contours of the individual regions of high and low vorticity.) The plume here seems to have narrowed down slightly. For the heating values of $G = 0.05$ and 0.1, as we have seen in earlier pictures of the velocity field, the acceleration appears to be so high that the plume-head has moved rapidly away from the rest of the plume.

A relaminarization-like behaviour is observed in the region of off-source heating.

4.6.3 Temporal Evolution of Flow Variables

The simulations reported above contain considerable information about the evolution of the starting plume with and without off source heating. Although in each case we have only one realization, certain characteristics of the evolution will be seen to stand out.

We shall present below data on axial variation of selected flow variables with no heating ($G = 0$) and with the maximum heating used in the simulations ($G = 0.1$).

Figures 4.12 to 4.14 show the results with no heating at t = 22, 28 and 35. The following are the salient features revealed by the figures.

- Figure 4.12, showing the azimuthal component of the velocity $u_{\theta c}$ is an indicator of where transition to turbulent flow occurs. From the figure this would appear to be at $z/d_0 \approx 2.5$, beyond which the amplitude of the fluctuating u_θ increases rapidly.

- Figure 4.13 shows u_{zc}, whose streamwise variations appear quite large. It is seen that at later times u_{zc} appears to be generally higher than at $t^* = 22$. The general nature of the variation suggests an association with the passage of the plume head. It is possible to recognize the location of the plume-head at each value of t^* by the presence of the peak velocities.

- Figure 4.14 shows $|\omega|$, which reaches high values around $z/d_0 = 2$ to 6, the peaks again corresponding to the plume head.

We shall now consider the solution at $G = 0.1$ and present distributions at $t = 22, 24$ and 28.

- First of all Figure 4.15 shows the evolution of the temperature at the center-line. Note that the highest values occur about 1 diameter after the end of the heat injection zone.

- Figure 4.16 shows $u_{\theta c}$. The fluctuations increase after transition at $z/d_o = 2.5$, go down in the heat injection zone and increase thereafter at $t^* = 28$.

- Figure 4.17 shows a dramatic increase in u_{zc} at $t^* = 28$ about one diameter after the injection of heat roughly where the temperature is also highest.

- Figure 4.18 shows that ω_z has its lowest values in the heat injection zone.

- Figure 4.19 shows that the trend of absolute vorticity from $z/d_0 = 0$ to 8 is a general decrease. Although we cannot define in any rigorous way the mean value of any flow variable in the starting plume, we note here that the scaling for the similarity solution for the steady turbulent plume suggests that the vorticity scale decreases with streamwise distance like $z^{-\frac{4}{3}}$ (the thickness goes like z and the centre-line velocity like $z^{-\frac{1}{3}}$. The general trend of the vorticity field till the beginning of the heat injection zone is therefore as expected. With heat addition the vorticity values shoot up. There is considerable generation of vorticity towards the end of and beyond the upper boundary of the heat injection zone.

Movies showing the time evolution of the azimuthal vorticity for different levels of heating are available in the compact disc attached to the thesis.

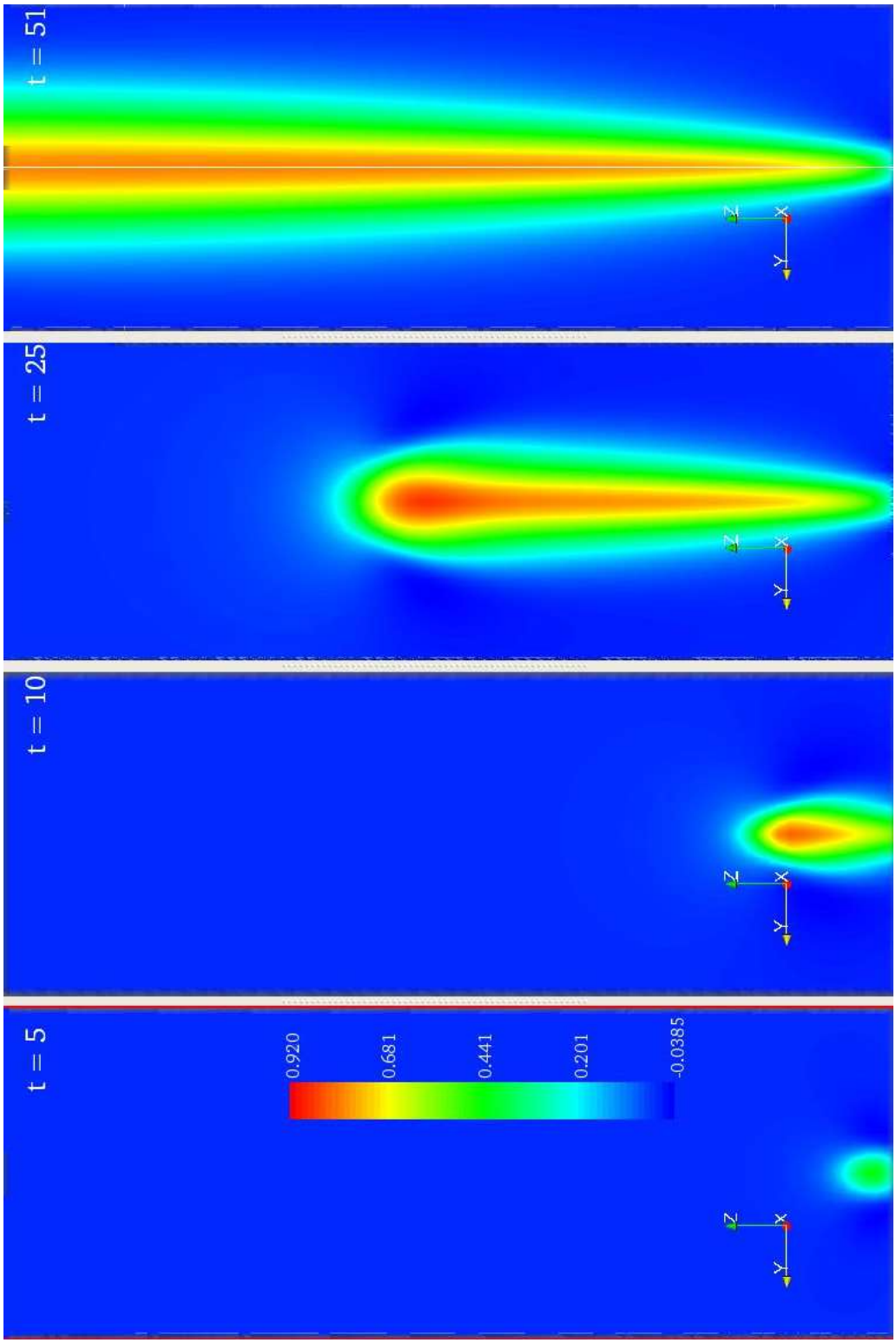

Figure 4.1: Contours of u_z velocity in laminar plume.

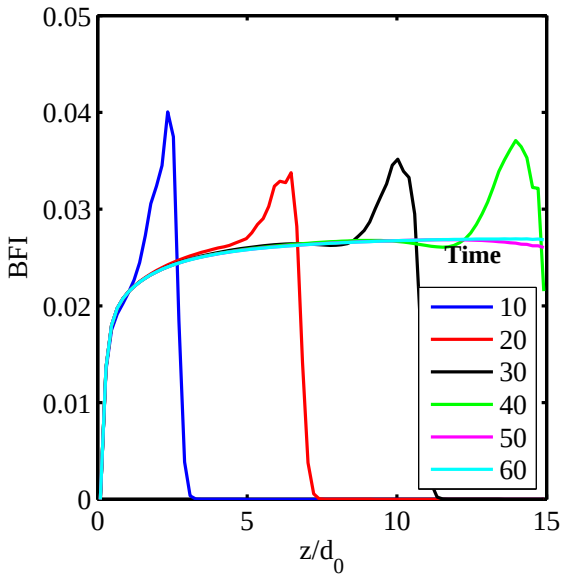

Figure 4.2: Plot of buoyancy flux integral along streamwise coordinate at different times.

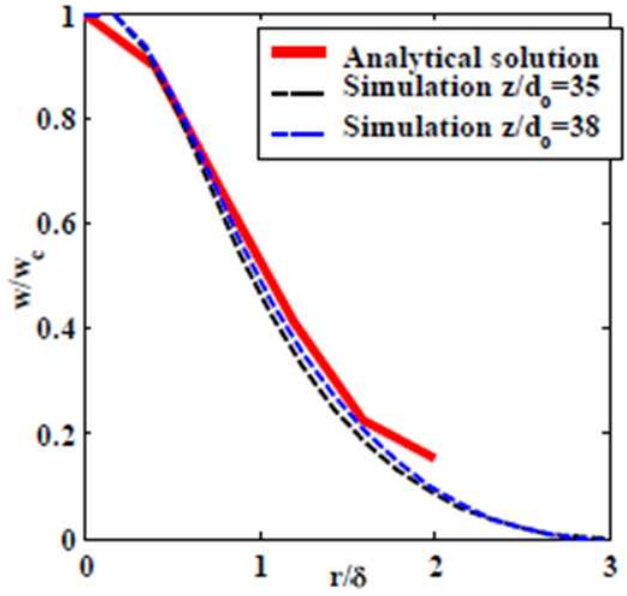

Figure 4.3: Velocity profile plotted along the radial direction.

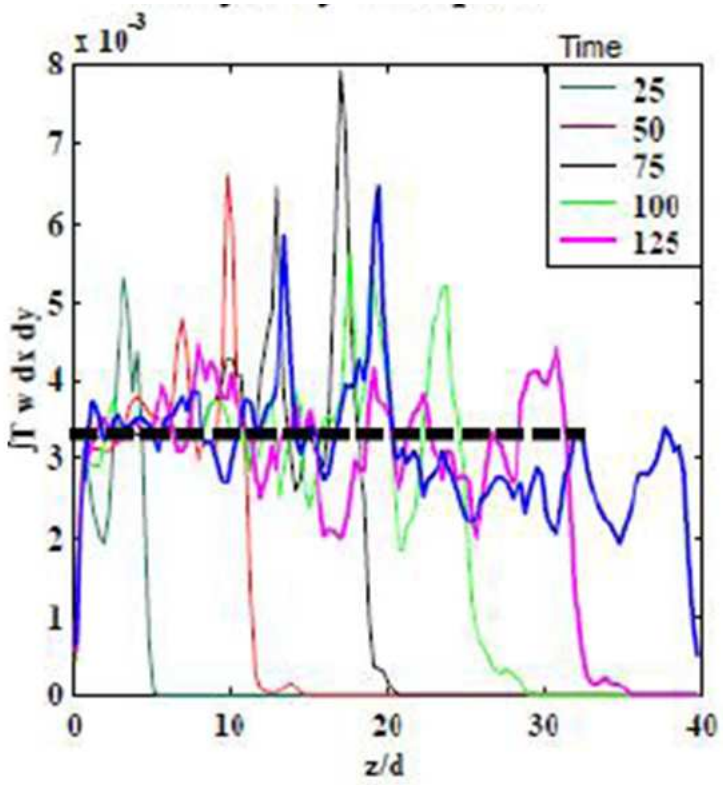

Figure 4.4: Plot of buoyancy flux integral along streamwise coordinate at different times.

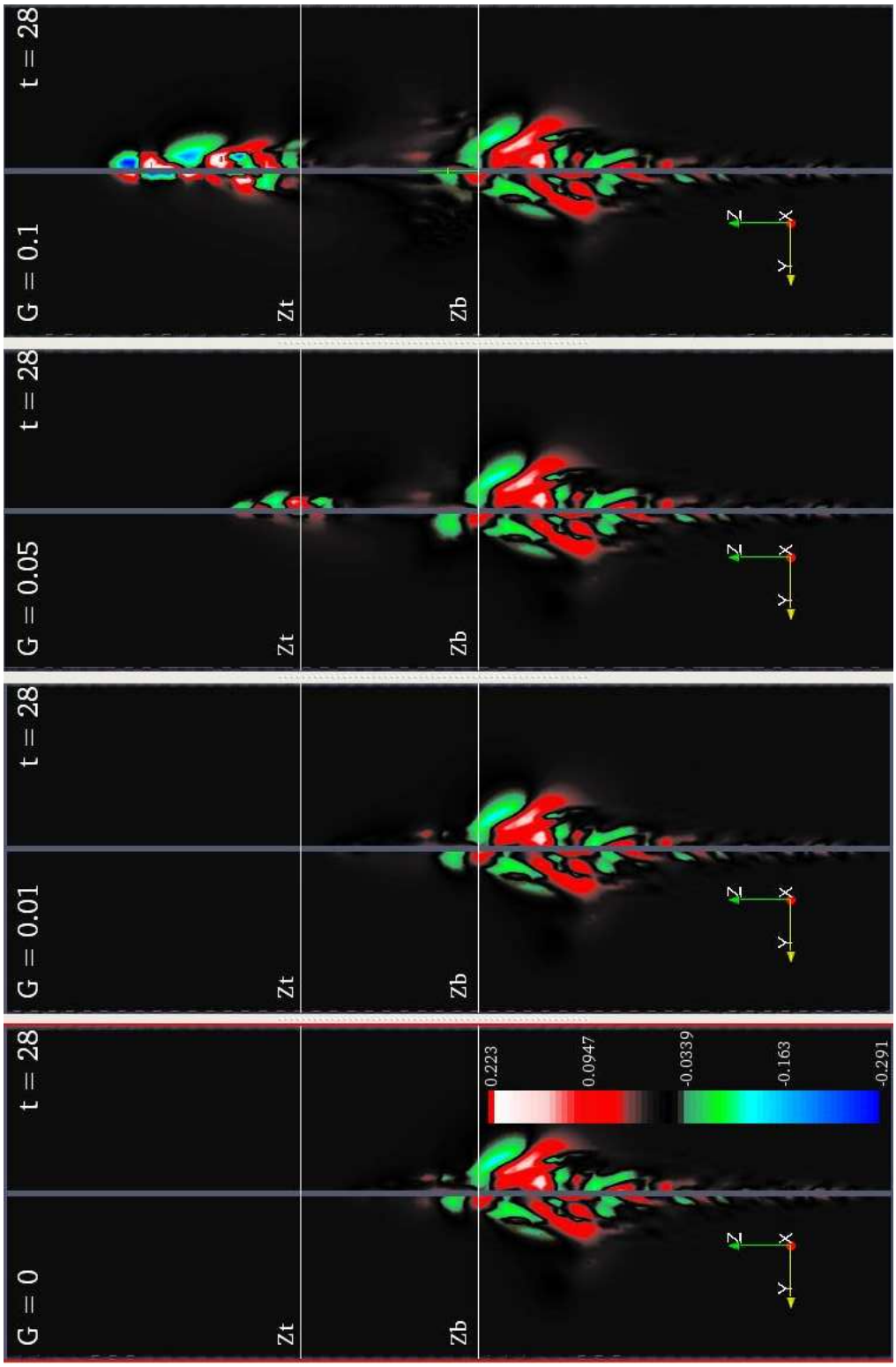

Figure 4.5: Contours of u_θ at $t^* = 28$ and $x = 0$ for different G values.

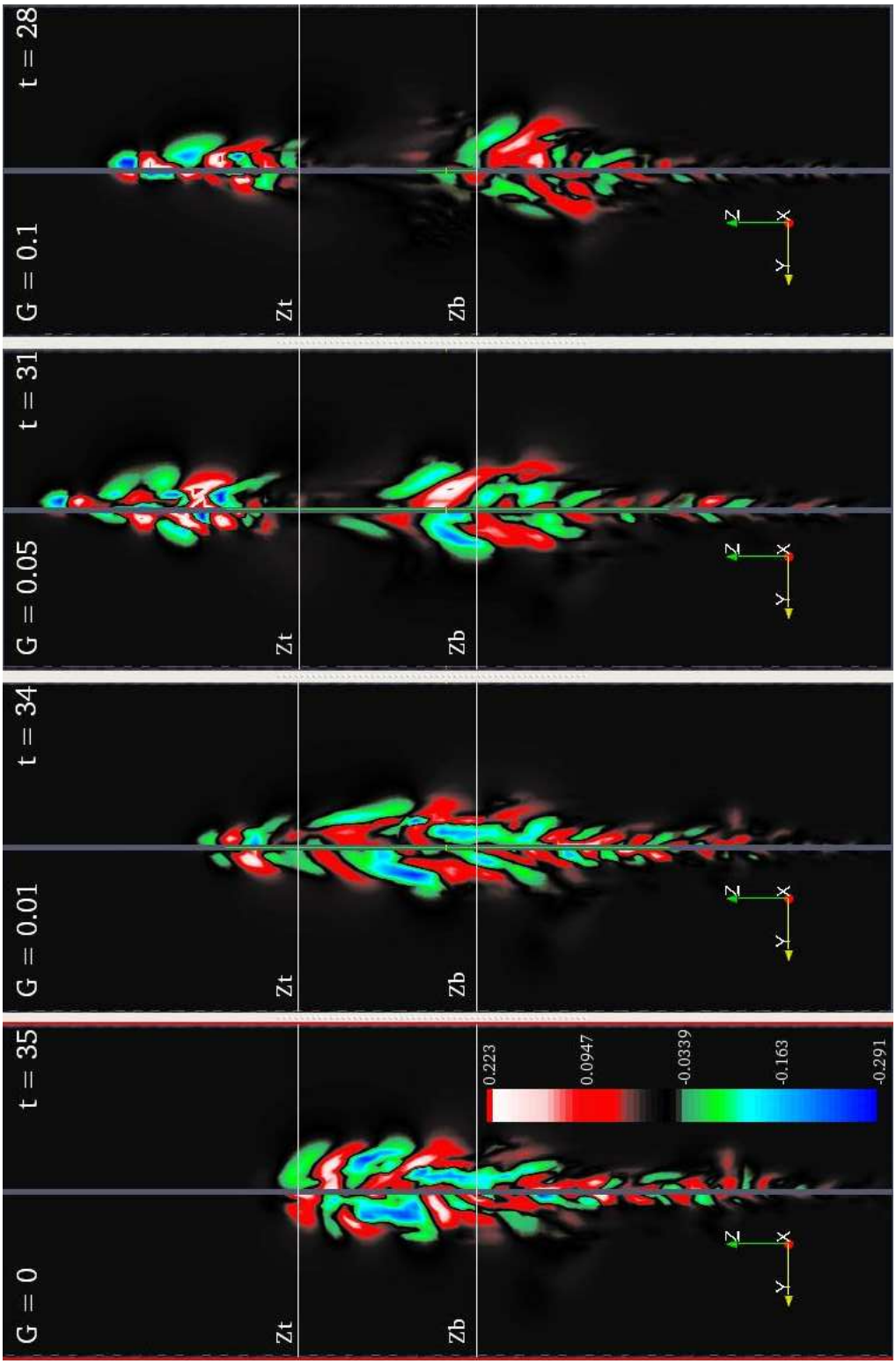

Figure 4.6: Contours of u_θ at $x = 0$ for different G values.

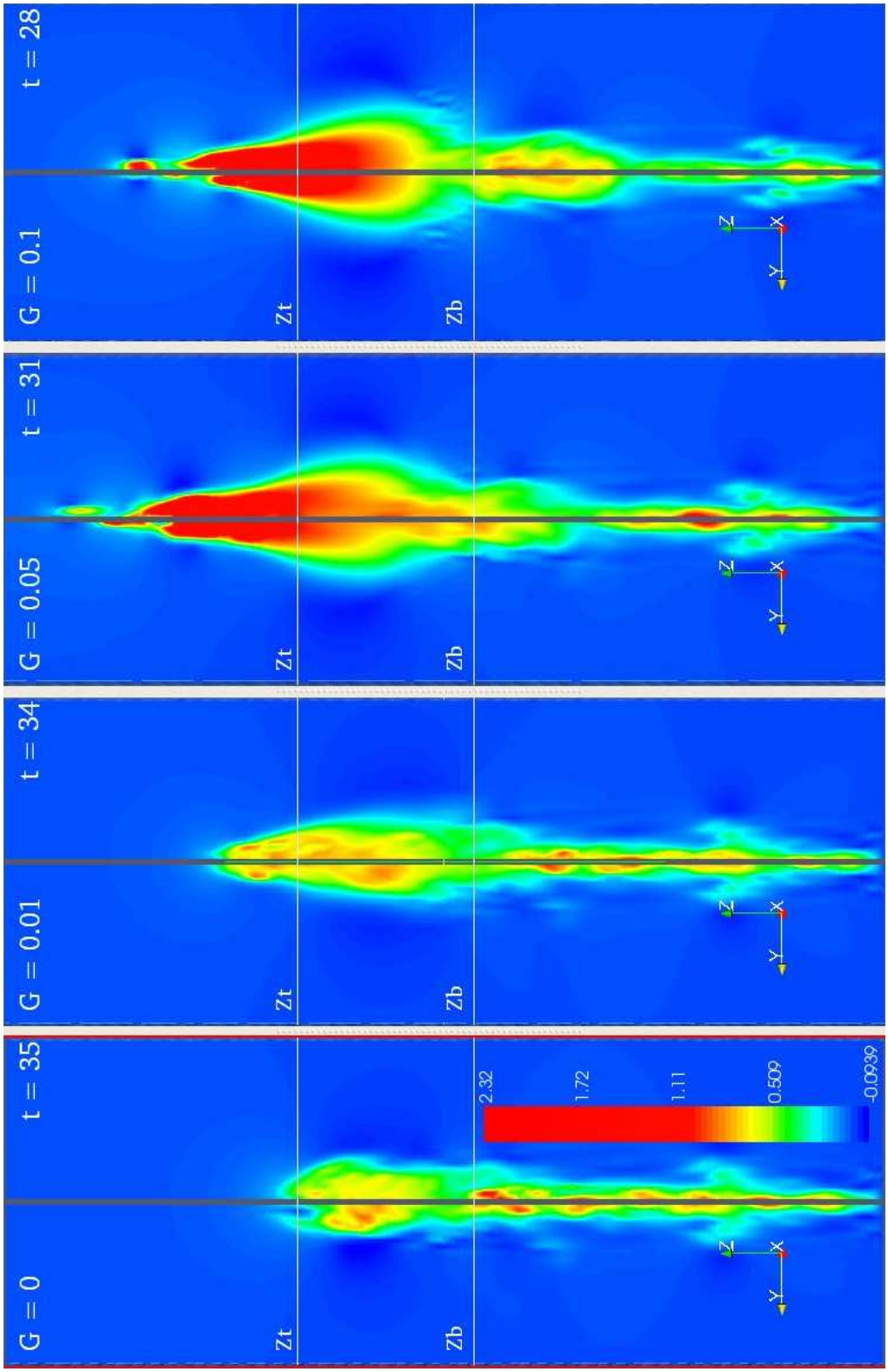

Figure 4.7: Contours of u_z at $x = 0$ for different G values.

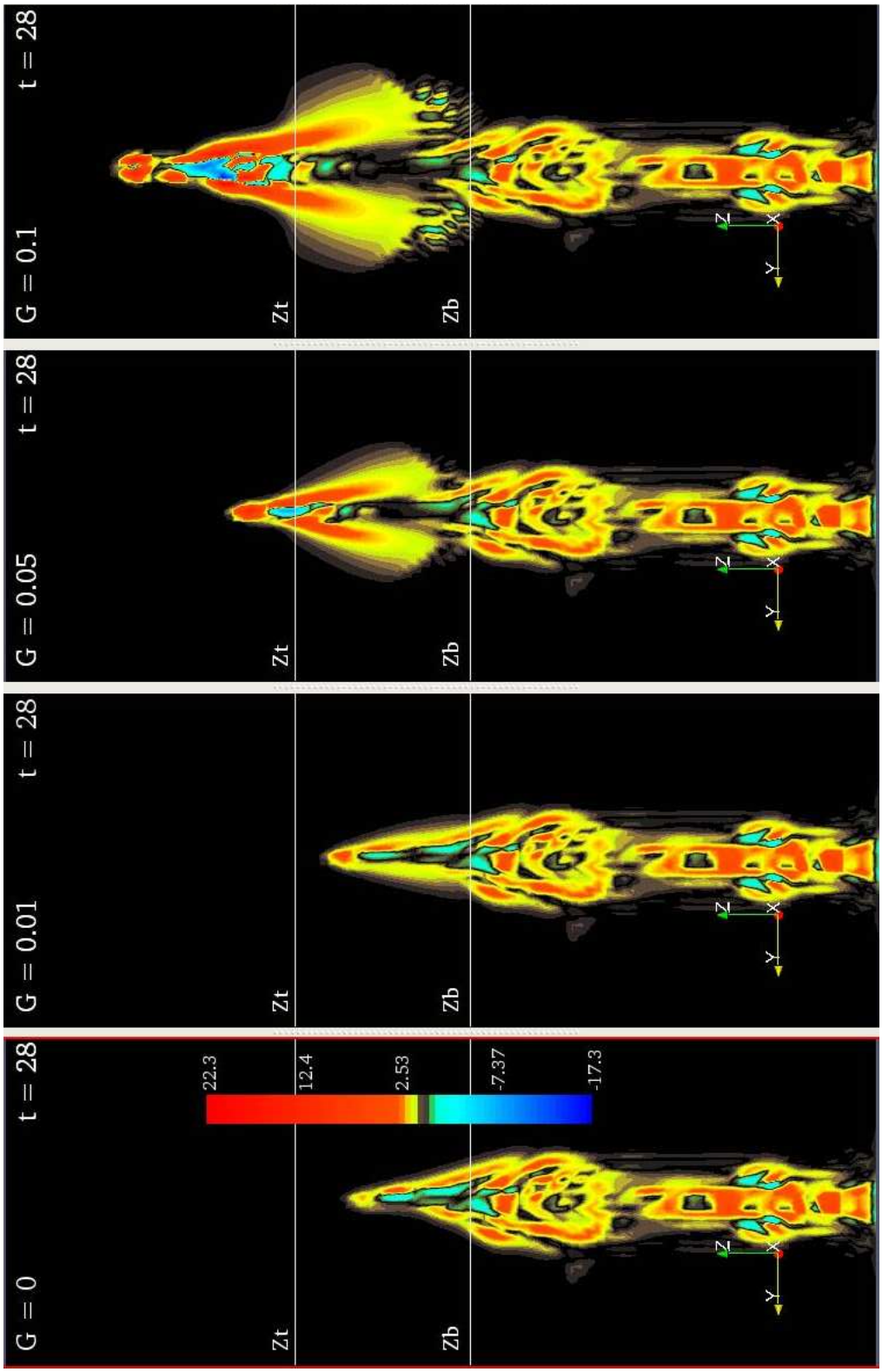

Figure 4.8: Contours of ω_θ at $t^* = 28$ and $x = 0$ for different G values.

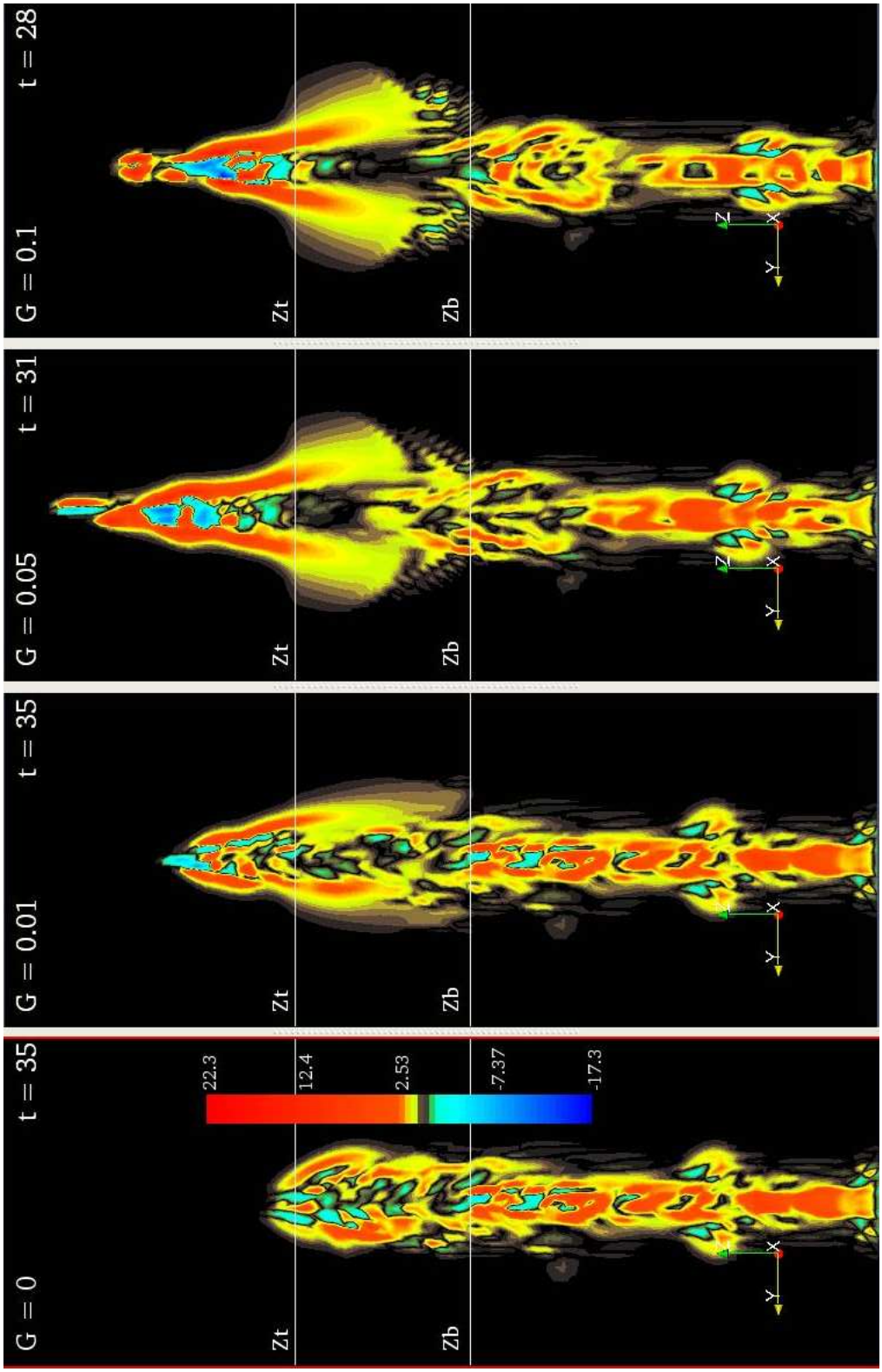

Figure 4.9: Contours of ω_θ at $x = 0$ for different G values.

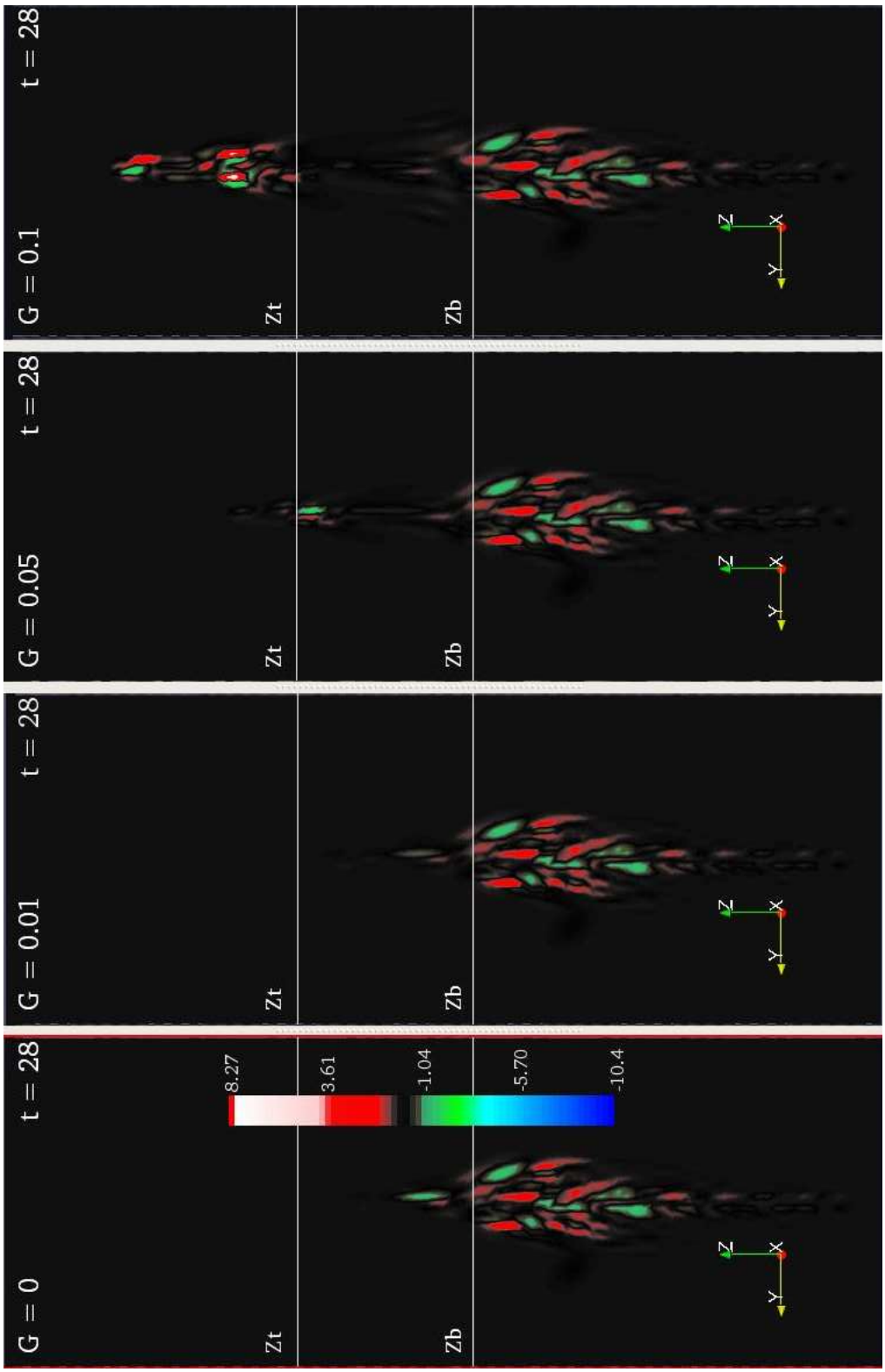

Figure 4.10: Contours of ω_z at $t^* = 28$ and $x = 0$ for different G values.

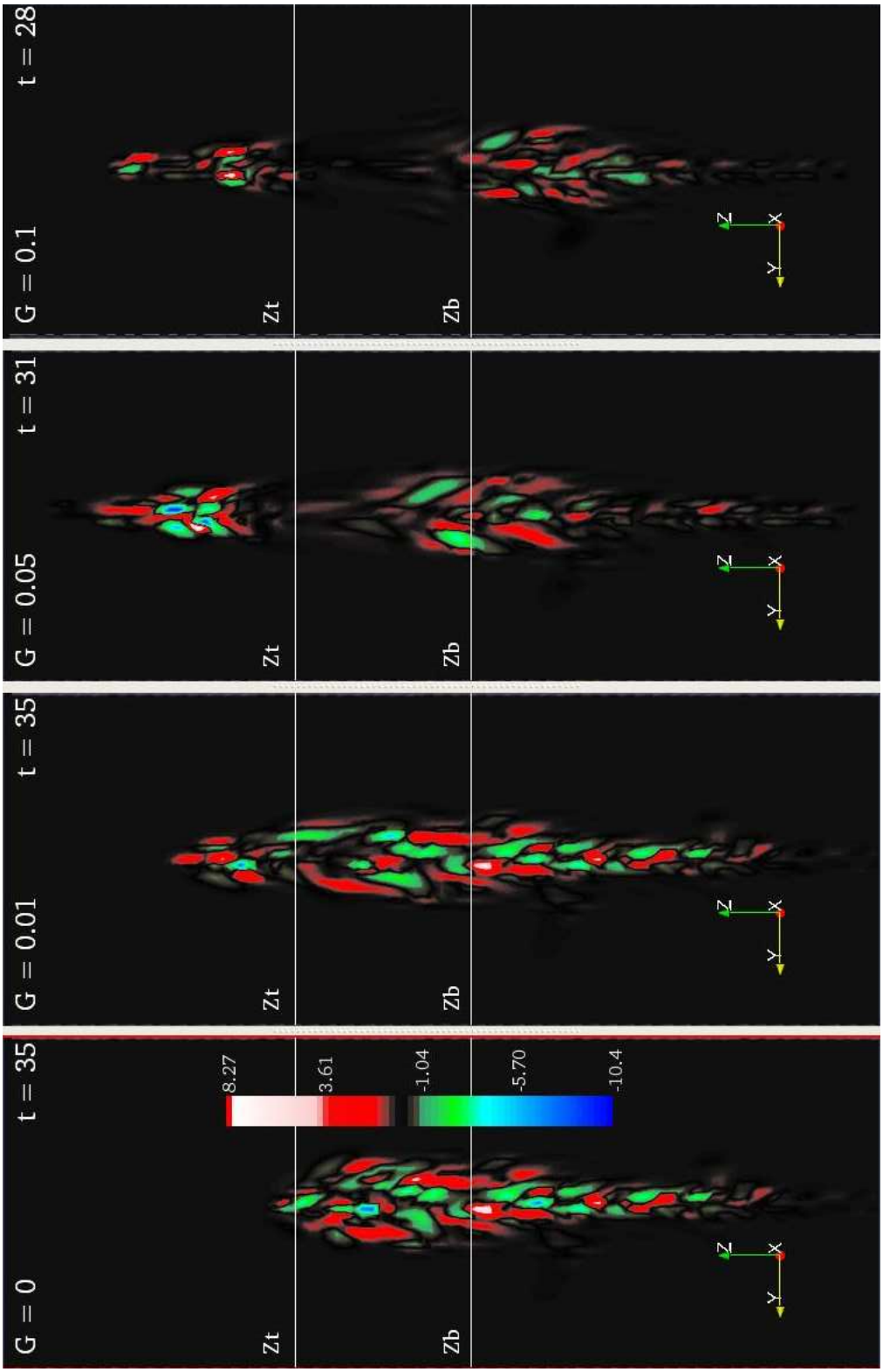

Figure 4.11: Contours of ω_z at $x = 0$ for different G values.

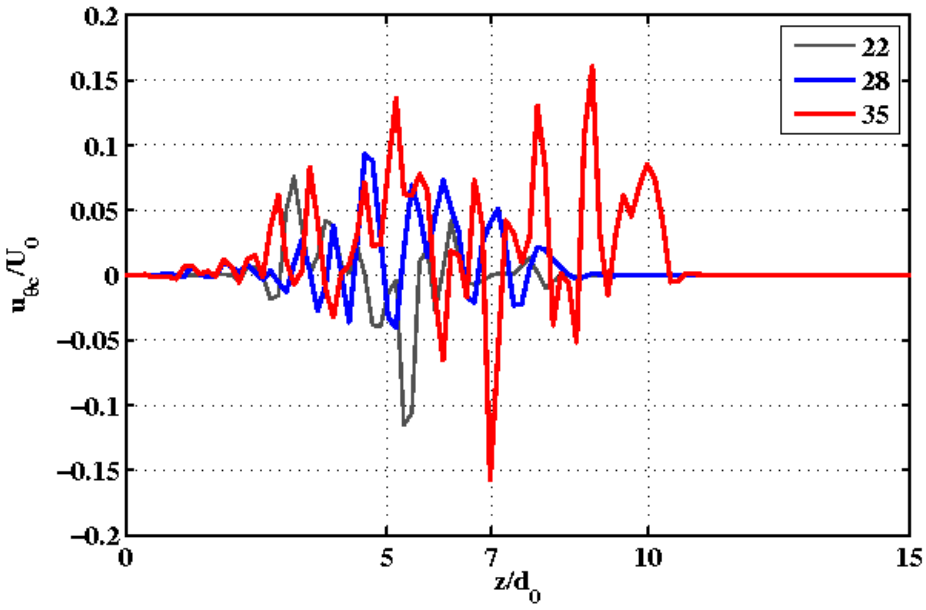

Figure 4.12: Plot of azimuthal velocity for an unheated plume along the streamwise coordinate for different times.

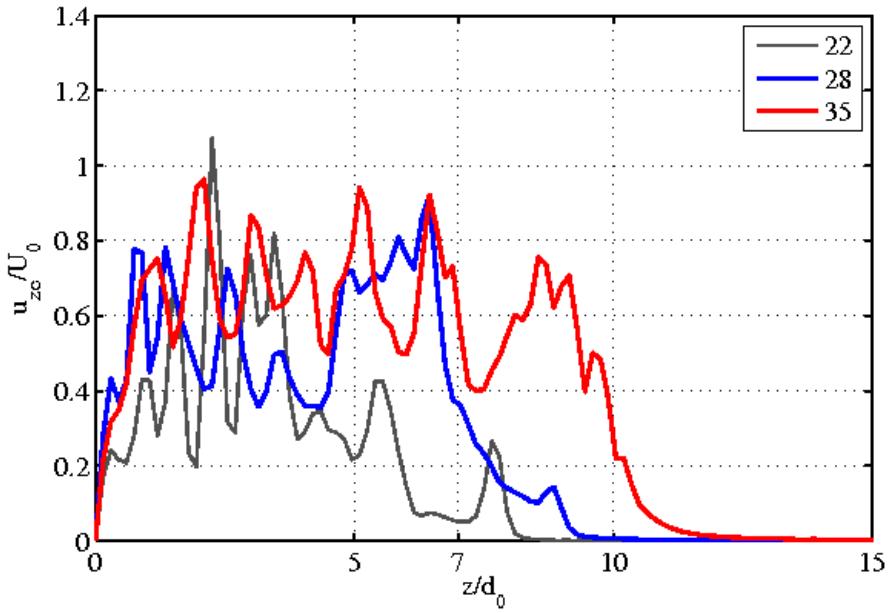

Figure 4.13: Plot of axial center-line velocity for an unheated plume along the streamwise coordinate for different times.

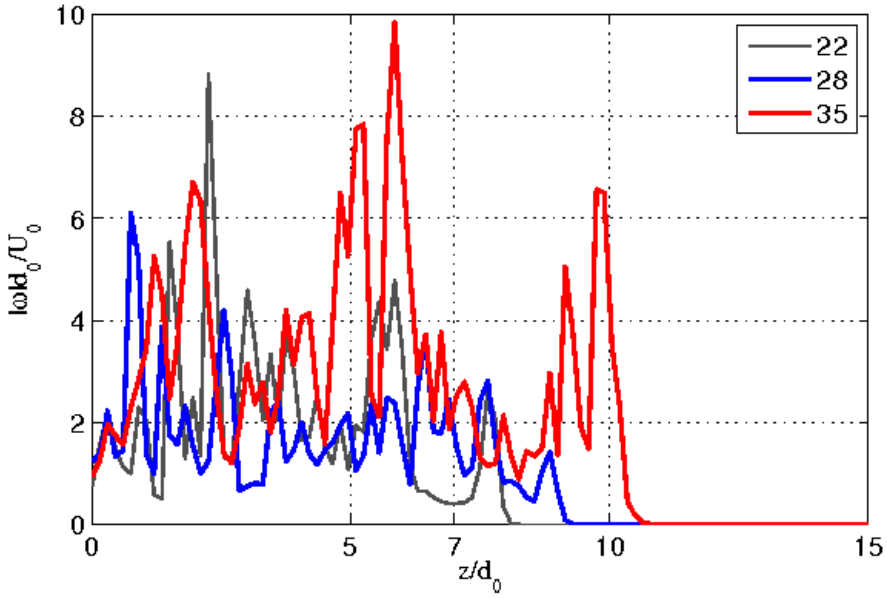

Figure 4.14: Plot of absolute vorticity at center-line for an unheated plume along the streamwise coordinate for different times.

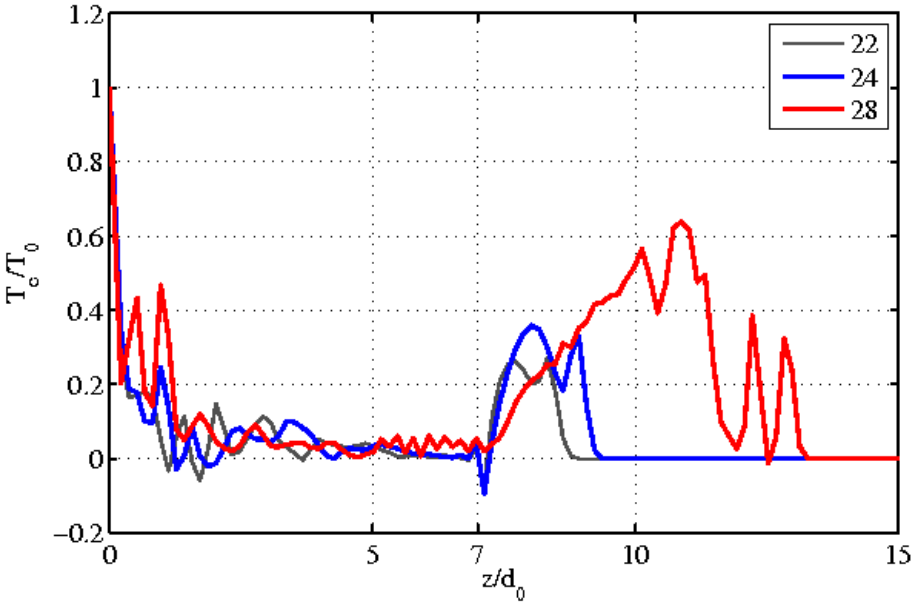

Figure 4.15: Plot of center-line temperature for a heated plume ($G = 0.1$) along the streamwise coordinate for different times.

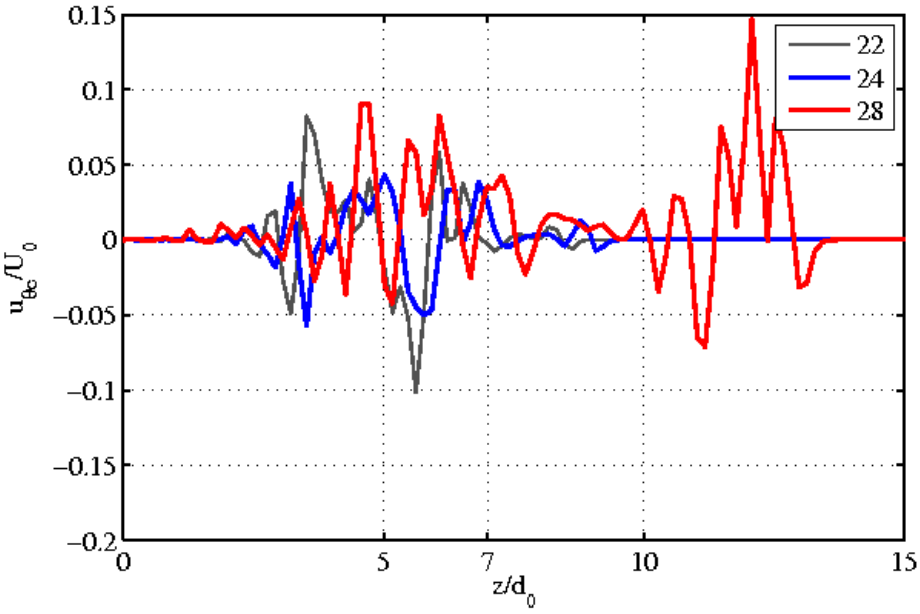

Figure 4.16: Plot of azimuthal velocity for a heated plume ($G = 0.1$) along the streamwise coordinate for different times.

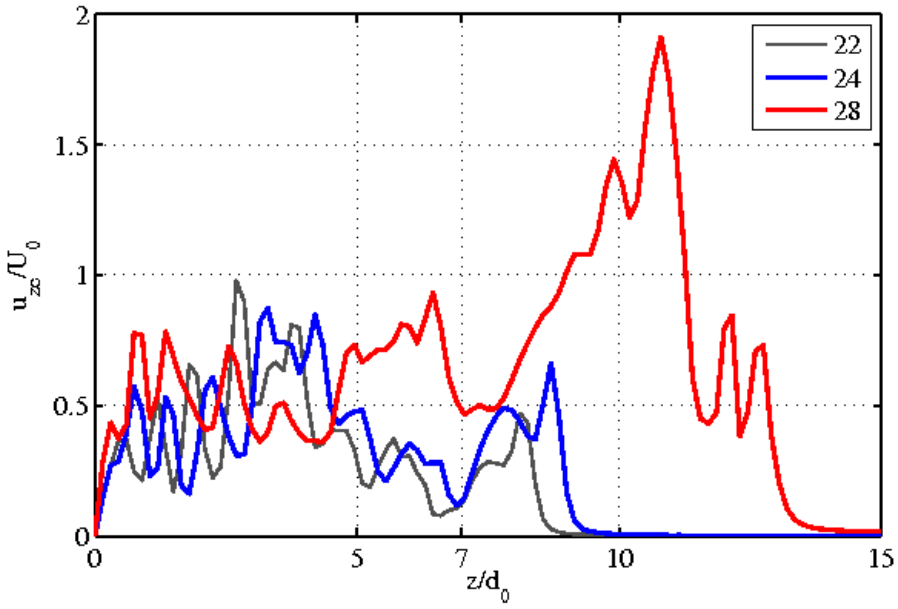

Figure 4.17: Plot of axial center-line velocity for a heated plume ($G = 0.1$) along the streamwise coordinate for different times.

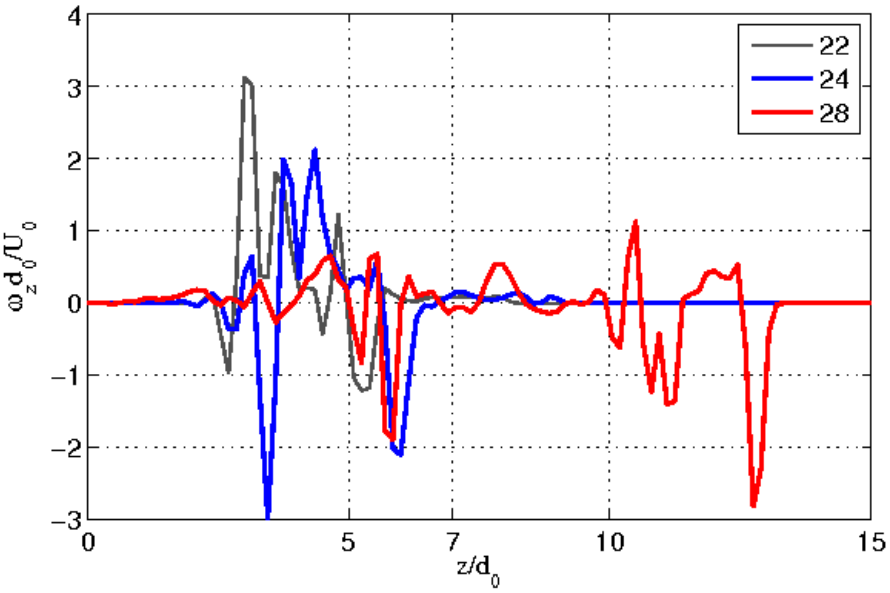

Figure 4.18: Plot of axial vorticity at center-line for a heated plume ($G = 0.1$) along the streamwise coordinate for different times.

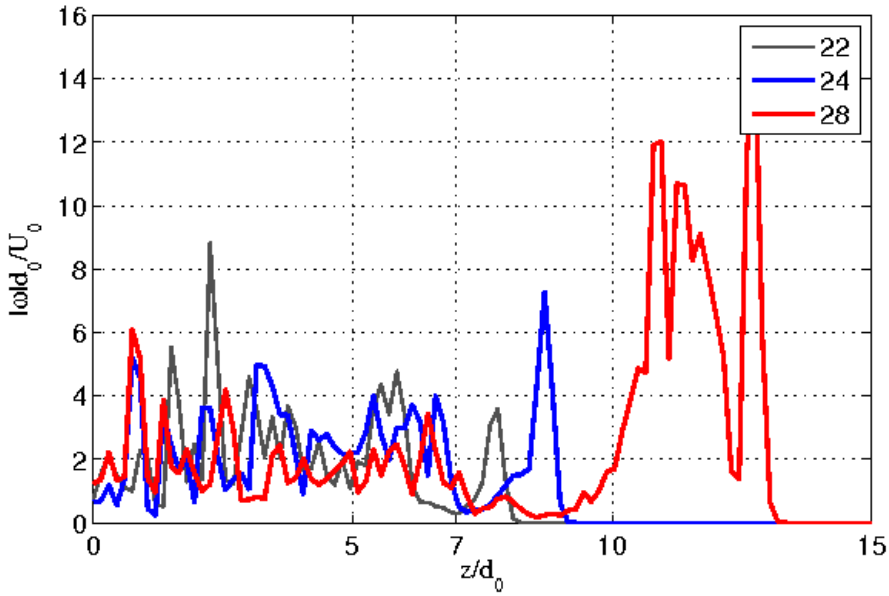

Figure 4.19: Plot of absolute vorticity at center-line for a heated plume ($G = 0.1$) along the streamwise coordinate for different times.

CHAPTER 5

CONCLUSIONS AND FUTURE WORK

In this thesis, we have carried out 2D and 3D direct numerical simulation of a starting plume with and without off-source volumetric heating, in an attempt to understand the fluid dynamics of cloud flows.

The 2D simulations show that volumetric heating leads to disruption of large scale structures at the lateral edges of the plume. In the heated plume, there is a drastic increase in the vorticity and we observe a protected core with no clear lateral boundary between the plume and the ambient fluid, consistent with previous experimental work on cloud flows. A reduction in entrainment of ambient fluid is seen in the heat injection zone, suggesting that these effects of volumetric heating are present also in a two-dimensional phenomenon.

A 3D DNS code which is parallelized using domain decomposition has also been developed to study starting plumes. We have found that zero vorticity at the lateral boundary and $\frac{\partial r u_r}{\partial r} = 0$, and zero normal derivate condition at the outflow boundary, are most appropriate for simulating this type of flow. A novel method has been used for parallelizing the code, using minimum physical memory and optimized data communication between the processors. The results of the 3D simulations indicate a drastic change in the flow structure due to off-source heat addition. As heating is increased, the width of the plume-head narrows down. Heating leads to increase in the absolute value of vorticity in the plume-head. At higher values of heating, the plume-head accelerates through the HIZ and detaches from the core. A relaminarization-like behaviour is also observed.

Further data analysis of the present results and detailed parametric study need

to be carried out. In future a more careful prescription for off-source volumetric heating profiles needs to be explored.

References

Agrawal, A., Boersma, B. J. & Prasad, A. K. 2004 Direct numerical simulation of a turbulent axisymmetric jet with buoyancy induced acceleration. *Flow Turbulence and Combustion* **73**, 277–305.

Agrawal, A. & Prasad, A. K. 2004 Evolution of a turbulent jet subjected to volumetric heating. *J. Fluid Mech.* **511**, 95–123.

Armfield, S. & Street, R. 1999 The fractional-step method for the navier-stokes equations on staggered grids: The accuracy of three variations. *J. Comput. Phys.* **153**, 660–665.

Babu, P. C. & Mahesh, K. 2004 Upstream entrainment in numerical simulation of a spatially evolving round jets. *Phys. Fluids* **16**, 3699–3705.

Basu, A. J. & Narasimha, R. 1999 Direct numerical simulation of turbulent flows with cloud-like off-source heating. *J. Fluid Mech.* **385**, 199–228.

Bhat, G. S. & Narasimha, R. 1996 A volumetrically heated jet: large-eddy structure and entrainment charateristics. *J. Fluid Mech.* **325**, 303–330.

Bhat, G. S., Narasimha, R. & Arakeri, V. H. 1989 A new method of producing local enhancement of buoyancy in liquid flows. *Exp. Fluids* **7**, 99–102.

Boersma, B. J., Brethouwer, G. & Nieuwstadt, F. T. M. 1998 A numerical investigation on the effect of the inflow conditions on the self-similar region of a round jet. *Phys. Fluids* **10**, 899–909.

Chorin, A. J. 1968 Numerical solution of the navier-stokes equations. *Mathematics Computation* **22**, 745–762.

Elavarasan, R., Bhat, G. S., Narasimha, R. & Prabhu, A. 1995 An experimental study of a jet with local buoyancy enhancement. *Fluid Dynam. Res.* **16**, 189–202.

Emanuel, K. A. 1994 *Atmospheric Convection*. Oxford University Press.

Faure, S., Laminie, J. & Temam, R. 2008 Colocated finite volume schemes for fluid flows. *Commun. Comput. Phys.* **4**, 1–25.

Fuji, T. 1963 Theory of the steady laminar convection above a horizontal line heat source. *Int. J. Heat. Mass Transfer* **6**, 597–606.

Gebhart, B. 1973 Instability, transition and turbulence in buoyancy-induced flows. *Annu. rev. Fluid Mech.* **5**, 213–246.

Guermond, J. L., Minev, P. & Shen, J. 2006 An overview of projection method for incompressible flows. *Comput. Meth. Appl. Mech. Eng.* **195**, 6011–6045.

Harlow, F. H. & Welch, J. E. 1965 Numerical calculation of time dependent viscous incompressible flow for fluids with free surface. *Phys. Fluids* **8**, 2182–2189.

List, E. 1982 Turbulent jets and plumes. *Annu. Rev. Fluid Mech.* **14**, 189–212.

Liu, M., Ren, Y. & Zhang, H. 2004 A class of fully second order accurate projection methods for solving the incompressible navier stokes equations. *J. Comp. Phys.* **200**, 325–346.

Morton, B. R., Taylor, G. I. & Turner, J. 1956 Turbulent gravitational convention from maintained and instantaneous sources. *Proc. R. Soc. London, Ser. A* **200**, 325–346.

Narasimha, R. & Bhat, G. S. 2008 Recent experimental and computational studies related to the fluid dynamics of clouds. *Computational Physics and New Perspectives in Turbulence, Proceedings IUTAM Symposium Nagoya, Japan* **Y. Kaneda (ed.), Springer, Netherlands**, 313–320.

Paluch, I. R. 1979 The entrainment mechanism in colorado cumuli. *J. Atmos. Sci.* **36**, 2467–2478.

Patankar, S. V. 1980 *Numerical Heat Transfer and Fluid Flow*. Series on Computational Methods in Mechanics and Thermal Science.

Plourde, F., Pham, M., Kim, S. D. & Balachandar, S. 2008 Direct numerical simulation of a rapidly expanding thermal plume: structure and entrainment interaction. *J. Fluid Mech.* **604**, 99–123.

Riehl, H. 1972 *Climate and Weather in the Tropics*. WMO Note 359.

Schneider, W. 1981 Flow induced by jets and plumes. *J. Fluid Mech.* **108**, 55–65.

Simpson, J. 1983 Cumulus clouds: earlyaircraft observations and entrainment hypotheses. *Mesoscale Meteorology* **T. Gal-Chen (ed.), D. Reidel, Netherlands**, 355–445.

Squires, P. & Turner, J. 1962 An entraining jet model for cumulonimbus updrafts. *Tellus* **14**, 422–434.

Sreenivas, K. R. 2004 Study of entrainment process in a planar jet using diffusion-vortex method. *Proceedings of the Tenth Asian Congress of Fluid Mechanics* **1**, 1–6.

Sreenivas, K. R. & Prasad, A. K. 2000 Vortex-dynamics model for entrainment in jets and plumes. *Phys. Fluids* **12**, 2101–2107.

Temam, R. 1969 Sur lápproximation de la solution des equations de navier-stokes par la method des pas fractionnaires ii. *Arch. Rat. Mech. Anal.* **33**, 377–385.

Turner, J. 1969 Buoyant plumes and thermals. *Annu. Rev. Fluid Mech.* **1**, 29–44.

Turner, J. 1986 Turbulent entrainment: the development of the entrainment assumption, and its application geophysical flows. *J. Fluid Mech.* **173**, 431–471.

Turner, J. S. 1973 *Buoyancy Effects in Fluids*. Cambridge University Press.

Van Kan, J. 1986 A second-order accurate pressure-correction scheme for viscous incompressible flow. *SIAM J. Sci. Stat. Comput.* **7**, 870–891.

Venkatakrishnan, L., Bhat, G. S. & Narasimha, R. 1999 Experiments on a plume with off-source heating: Implications for cloud fluid dynamics. *J. Geo. Res.* **104**, 14271–14281.

Venkatakrishnan, L., Elavarasan, R., Bhat, G. S., Krothapalli, A. & Laurenco, L. 2003 Experiments on a plume with off-source heating; implications for cloud. *Curr. Sci.* **85**, 597–606.

Verzicco, R. & Orlandi, P. 1996 A finite-difference scheme for three-dimensional incomprresible flows in cylindrical coordinates. *J. Comput. Phys.* **123**, 402–414.

Warner, J. 1970 On steady-state one-dimensional models of cumulus convection. *J. Atmos. Sci.* **27**, 1035–1040.

Yih, C. & Wu, F. 1981 Round buoyant laminar and turbulent plumes. *Phys. Fluids* **24**, 794–801.